

Magnetospherically reflected, specularly reflected, and backscattered whistler mode radio-sounder echoes observed on the IMAGE satellite:

1. Observations and interpretation

V. S. Sonwalkar,¹ D. L. Carpenter,² A. Reddy,¹ R. Proddaturi,¹ S. Hazra,¹ K. Mayank,¹ and B. W. Reinisch³

Received 17 April 2011; revised 27 July 2011; accepted 11 August 2011; published 11 November 2011.

[1] A survey of echoes detected in 2004–2005 during pulse transmissions from the Radio Plasma Imager (RPI) instrument on the IMAGE satellite has revealed several new features of sounder generated whistler mode (WM) echoes and has indicated ways in which the echoes may be used for remote sensing of the Earth's plasma structure at altitudes <5000 km. In this paper we describe the frequency versus travel time ($f - t$) forms of the WM echoes as they appear on RPI plasmagrams and discuss qualitatively their raypaths and diagnostic potentials. Based on their reflection mechanism, the WM echoes can be classified as: magnetospherically reflected (MR), specularly reflected (SR), or backscattered (BS). The MR echoes are reflected at altitudes where the local lower hybrid frequency (f_{lh}) is equal to the transmitted pulse frequency f , a phenomenon familiar from both theory and passive recordings of WM wave activity. The SR echoes (previously reported in a higher frequency range) are reflected at the Earth-ionosphere boundary, either with wave vector at normal incidence or, more commonly (and unexpectedly, due to ray bending in the layered ionosphere), at oblique incidence. The BS echoes are the result of scattering from small scale size plasma density irregularities close to IMAGE. The echoes are described as discrete, multipath, and diffuse, depending upon the amount of travel-time spreading caused by the presence of field aligned density irregularities (FAIs) along echo raypaths. The WM echoes described in this paper have been observed at altitudes less than 5,000 km and at all latitudes and at most MLTs. The diagnostic potential of these phenomena for remotely studying the distribution of plasma density and composition along the geomagnetic field line \mathbf{B}_0 , as well as the presence of FAIs of varying scale sizes, is enhanced by the tendency for SR and MR echoes to be observed simultaneously along with the upward propagating signals from a spatial distribution of communication VLF transmitters. We believe that our findings about WM propagation and echoing in an irregular medium have important implications for the connection between WM waves and the Earth's radiation belts. In a companion paper by *Sonwalkar et al.* (2011), we employ ray tracing and refractive index diagrams in quantitative support of this paper and also present two diagnostic case studies of plasma density, ion effective mass, and ion composition along \mathbf{B}_0 .

Citation: Sonwalkar, V. S., D. L. Carpenter, A. Reddy, R. Proddaturi, S. Hazra, K. Mayank, and B. W. Reinisch (2011), Magnetospherically reflected, specularly reflected, and backscattered whistler mode radio-sounder echoes observed on the IMAGE satellite: 1. Observations and interpretation, *J. Geophys. Res.*, 116, A11210, doi:10.1029/2011JA016759.

¹Electrical and Computer Engineering Department, University of Alaska Fairbanks, Fairbanks, Alaska, USA.

²Space, Telecommunications and Radioscience Laboratory, Stanford University, Stanford, California, USA.

³Center for Atmospheric Research, University of Massachusetts Lowell, Lowell, Massachusetts, USA.

1. Introduction

[2] This paper presents new observations and interpretation of whistler mode (WM) echoes of pulses transmitted by the Radio Plasma Imager (RPI) [*Reinisch et al.*, 2000] on the IMAGE satellite [*Burch*, 2000] when operating at altitudes <5000 km. These sounding operations have allowed us to observe the results of WM sounding in an altitude range not previously explored and at frequencies lower than those previously employed. In making preliminary assessments of

the new data, we are able to draw upon existing knowledge of several important whistler mode propagation phenomena, notably (1) non-ducted propagation, wherein wave-normal directions are not constrained to remain within a small cone of angles around the direction of the geomagnetic field but are strongly affected by large-scale spatial variations of the plasma parameters [e.g., *Walter and Angerami*, 1969; *James*, 1972; *Cerisier*, 1973; *Sonwalkar et al.*, 1984], (2) the phenomenon of “magnetospheric reflection” (MR), in which the raypath of a wave propagating at large wave-normal angle is reversed near a point where the refractive index surface undergoes an important change in topology and size (e.g., *Kimura* [1966], *Smith and Angerami* [1968], who introduced the term “magnetospheric reflection,” *Edgar* [1976], and *Shklyar et al.* [2010]), (3) spreading of wave-normals (and hence time delays) due to encounters with geomagnetic field aligned density irregularities (FAIs) of transverse scale sizes varying from 10 m to 100 km [e.g., *James*, 1972; *Sonwalkar et al.*, 1984, 2004a], and (4) partial or complete reflection of downcoming waves at the sharp lower ionospheric boundary [e.g., *Helliwell*, 1965; *Brittain et al.*, 1983; *Sonwalkar et al.*, 2004a].

[3] In this paper we discuss how evidence of these phenomena in IMAGE sounding data suggest a new method of studying poorly known aspects of the altitude distribution of ion composition and of the occurrence of FAIs between ~90 km and ~5000 km. We show how a variety of WM echoes appear on sounder records and qualitatively review the physical mechanisms believed responsible for their occurrence. In a companion paper, *Sonwalkar et al.* [2011, hereinafter Paper II] use ray tracing simulations to provide quantitative explanations of observed echo properties and illustrate the proposed new method of studying electron and ion (H^+ , He^+ , O^+) densities along the field line passing through the satellite.

[4] The RPI instrument (3 kHz – 3 MHz) on IMAGE (~1000 km \times 7.2 R_E altitude polar orbit) permitted sounding experiments in the free-space-, Z-, and whistler- mode domains [*Reinisch et al.*, 2000; *Burch*, 2000]. The first observations of WM echoes on IMAGE [*Sonwalkar et al.*, 2004a] included discrete and multipath echoes specularly reflected (SR) from the Earth-ionosphere boundary and diffuse echoes backscattered (BS) by small scale field-aligned irregularities present near IMAGE. This paper describes several new features of SR and diffuse echoes not noted earlier. For example, we show that SR echoes fall into two categories: (1) a normally incident (NI) echo that retraces its propagation path after reflecting at the Earth-ionosphere boundary, and (2) an obliquely incident (OI) echo whose propagation path forms a loop. Furthermore, we identify magnetospherically reflected echo forms that are confined to frequencies below ~15 kHz and have not previously been identified on sounder records. The WM echoes described in this paper have been observed at altitudes less than 5,000 km and at all latitudes and at most MLTs.

[5] The measured dispersions (time delay versus frequency) of SR and MR echoes are variously sensitive to the distribution of electrons and ions along their respective raypaths, in the SR case being primarily influenced by the electron density from the satellite altitude to the bottom of the ionosphere and in the MR case (also in the SR case within a

narrow range of frequencies) by both the electron density and ion composition down to the lowest reflection altitude reached. Meanwhile, the spread in time delays as a function of frequency of SR and MR echoes provides a method to detect the presence of FAIs along particular raypaths and in some cases to estimate their transverse scale sizes.

[6] The study of WM echoes on IMAGE is particularly important because for the first time we have such waves injected into the magnetosphere in all directions from a specific location in the magnetosphere. This is in direct contrast to the conditions under which waves are injected into space from the ground by lightning sources or VLF transmitters. These latter tend to be incident on the ionosphere over a range of latitudes and longitudes and at each point of penetration are confined in terms of wave-normal direction to a narrow cone of angles around the vertical (because of Snell’s law and the refractive index $\mu \gg 1$ in the ionosphere). Because of this fundamental difference between in situ and ground based wave injection (and hence in the paths that are followed by the injected waves), the unique possibilities for use of the former as probes of physical processes such as MR and SR reflection and scattering by FAIs deserve special recognition and have become the basis of this paper and its companion.

[7] The organization of this paper differs from the usual practice of describing observations and then offering interpretations of the data, as is customary when working on a ‘direct’ problem in radio probing of a region. Instead, because of the novelty and complexity of the data records, section 2 begins with qualitative descriptions of various propagation scenarios that our analysis (including ray tracing) suggests and are represented in the data. These descriptions are offered as predictions about what may be observed when a sounder injects waves into a region of interest at all wave-normal angles from a fixed location. The predictions are based upon use of an empirical model of the plasma environment below 4000 km, and draw upon the existing general knowledge of WM propagation mentioned above, upon limited earlier studies of WM echoes detected on IMAGE [*Sonwalkar et al.*, 2004a], and upon our analysis of the new data. Section 3 describes the RPI experiment and section 4 the observations and their preliminary interpretation in the light of the reflection mechanisms discussed in section 2. Section 5 offers a brief discussion and section 6 concluding remarks.

[8] The companion paper, Paper II, continues discussion of the ‘direct’ problem by recalling the physical principles of WM echo sounding and predicting the manner in which spatial variations in the WM refractive index will affect echo raypaths. Ray tracing simulations based on a diffusive equilibrium plasma density model are presented in quantitative support of the proposed MR and SR propagation mechanisms. The paper then deals with the ‘inverse’ problem, using two case studies to illustrate how the observed dispersions of MR and SR echoes, when combined with ray tracing, can provide information on electron density, density irregularities, and ion composition along the field line passing through IMAGE.

[9] The results reported in this and the companion paper were first presented at AGU 2006, 2007, 2008, and 2009 Fall conferences in San Francisco [*Sonwalkar et al.*, 2006,

2007, 2008b, 2009] and the 2008 URSI General Assembly in Chicago [Sonwalkar et al., 2008a].

2. A Qualitative Picture of the Production of Whistler Mode Echoes

2.1. Types of WM Echo Reflection

[10] Monostatic observation of a WM echo necessarily requires a reflection mechanism and a return path to the wave source. There are two distinctly different types of echo reflection, both of which (as detailed in Paper II) depend upon spatial changes in the refractive index along raypaths below or above the satellite.

[11] (1) For a wave at frequency f propagating at a wave-normal angle near 90° , magnetospheric reflection (MR) occurs at an altitude where the refractive index surface changes from an open to a closed topology. This can happen in a smoothly varying medium when the wave encounters the condition $f_{lh} \sim f$, where f_{lh} is the local lower hybrid resonance frequency [Kimura, 1966; Smith and Angerami, 1968; Edgar, 1976]. At reflection (properly viewed as a process of refraction), the ray direction becomes transverse to \mathbf{B}_0 as it changes from downward (upward) to upward (downward), thus describing a loop as the echo returns to the satellite.

[12] (2) For a wave at frequency f , propagating at small or large wave-normal angles, specular reflection (SR) occurs at the Earth-ionosphere boundary near 90 km for that wave that has not undergone a magnetospheric reflection discussed above. Near 90 km, the refractive index governing this wave undergoes an ‘abrupt’ change from the magnetized-plasma conditions of the bottomside ionosphere to the essentially free-space conditions of the earth-ionosphere waveguide [Helliwell, 1965]. We note that Muldrew [1969], from soundings between ~ 200 and 800 kHz on Alouette II, identified whistler mode echoes on a limited number of ionograms recorded at high latitudes in early morning as having reflected at the Earth’s surface.

[13] Incident upon the waveguide boundary, which need not be horizontally stratified, there will generally be a distribution of wave-normals and ray directions that depends on the amount of ray bending that has occurred as the waves (launched at various angles and hence onto various raypaths) penetrated the dense F layer. There may then occur two types of SR echo reflection, one involving a ray for which the wave-normal is normally incident on the boundary (the NI echo) and the other a ray whose wave-normal is obliquely incident (the OI echo). In the NI case, both the incident and reflected wave-normal angles are perpendicular to the boundary, and during reflection the ray direction is reversed such that the echo retraces its path to the satellite. For the OI case, in which the incident and reflected angles differ from one another (because of the anisotropy of the medium), the incident and reflected wave-normal angles are oblique, as are the incident and reflected ray directions. Thus the echo path to the satellite forms a loop. Although called specular, SR reflection may be understood to include penetration of the ionospheric lower boundary by a fraction of the incident wave energy. All waves that start from the satellite eventually undergo MR or SR reflection, but only some subset of them return in the form of observable echoes.

[14] In light of the key features of whistler mode propagation listed above and the possibility of radiation at a wide

range of wave-normal angles, what types of echoes may we expect to observe from a VLF transmitter operating near 4000 km, and in what frequency bands should the various types occur? Figure 1 provides a conceptual basis for answering these questions.

2.2. Conceptual Framework for Discussing the Echo Data

[15] Figure 1 provides the conceptual setting within which the WM echoes of interest are expected to occur.

[16] In a plasma composed of electrons, protons, and helium and oxygen ions, the expression for f_{lh} , plays a key role in any discussion of WM propagation, reflection, and echo formation.

$$\frac{1}{f_{lh}^2} = \left(\frac{m_p}{m_e} m_{eff} \right) \left(\frac{1}{f_{pe}^2} + \frac{1}{f_{ce}^2} \right) \quad (1)$$

where $m_p/m_e \approx 1836$ is the ratio of the proton mass to the electron mass and m_{eff} is the ion effective mass, defined below for a hydrogen (H^+), helium (He^+), and oxygen (O^+) plasma.

$$\frac{1}{m_{eff}} = \frac{\alpha_{H^+}}{1} + \frac{\alpha_{He^+}}{4} + \frac{\alpha_{O^+}}{16}, \quad (2)$$

where $\alpha_{H^+} = N_{H^+}/N_e$, $\alpha_{He^+} = N_{He^+}/N_e$, $\alpha_{O^+} = N_{O^+}/N_e$, are the fractional ion abundances and N_e , N_{H^+} , N_{He^+} , and N_{O^+} are the densities of electrons, H^+ , He^+ , and O^+ ions respectively.

[17] We assume that at low altitudes (< 5000 km), where most of the WM echoes on IMAGE have been observed, the magnetosphere may be described by a diffusive equilibrium density model and the dipole geomagnetic field (see Paper II). Figure 1a shows typical variations of plasma parameters, f_{pe} , f_{ce} , m_{eff} , and f_{lh} , along the field-line \mathbf{B}_0 passing through the satellite (the specific plasma density model shown in this figure was obtained from a ray tracing analysis of WM echoes observed on 22 October 2005, when the satellite was at $R_{Sat} = 3404$ km and $L = 2.13$ (see Paper II)). The frequency scale corresponding to f_{pe} and f_{ce} is shown above and the scale corresponding to f_{lh} (in kHz) and to m_{eff} (in amu) is shown below.

[18] With decreasing altitude, the gyrofrequency increases monotonically and the plasma frequency first increases down to the F2 layer peak near $R_{F2} = 215$ km after which it decreases monotonically down to the bottom of the ionosphere at $R_{Bot} = 90$ km. The ion effective mass increases monotonically, consistent with a diffusive equilibrium model in which the lighter ions (e.g. H^+ , He^+) are the principal constituents at higher altitudes and a heavier ion (e.g. O^+) is the principal constituent at lower altitudes. For typical magnetospheric parameters, $m_{eff} \sim 1$ above ~ 2000 km and then begins to increase with decreasing altitude, first slowly and then rapidly, reaching large values ($1 < m_{eff} < 16$) above the F2 layer and eventually reaching ~ 16 near the bottom of the ionosphere. From equation (1) we see that f_{lh} increases with f_{pe} and f_{ce} and decreases with m_{eff} . The net effect of the variations of these three parameters is that f_{lh} increases with decreasing altitude, reaches a maximum frequency $f_{lh,max1} \sim 10$ kHz at $R_{f_{lh,max1}} \sim 1400$ km, decreases to a minimum $f_{lh,min} \sim 6$ kHz at ~ 600 km, reaches another maximum

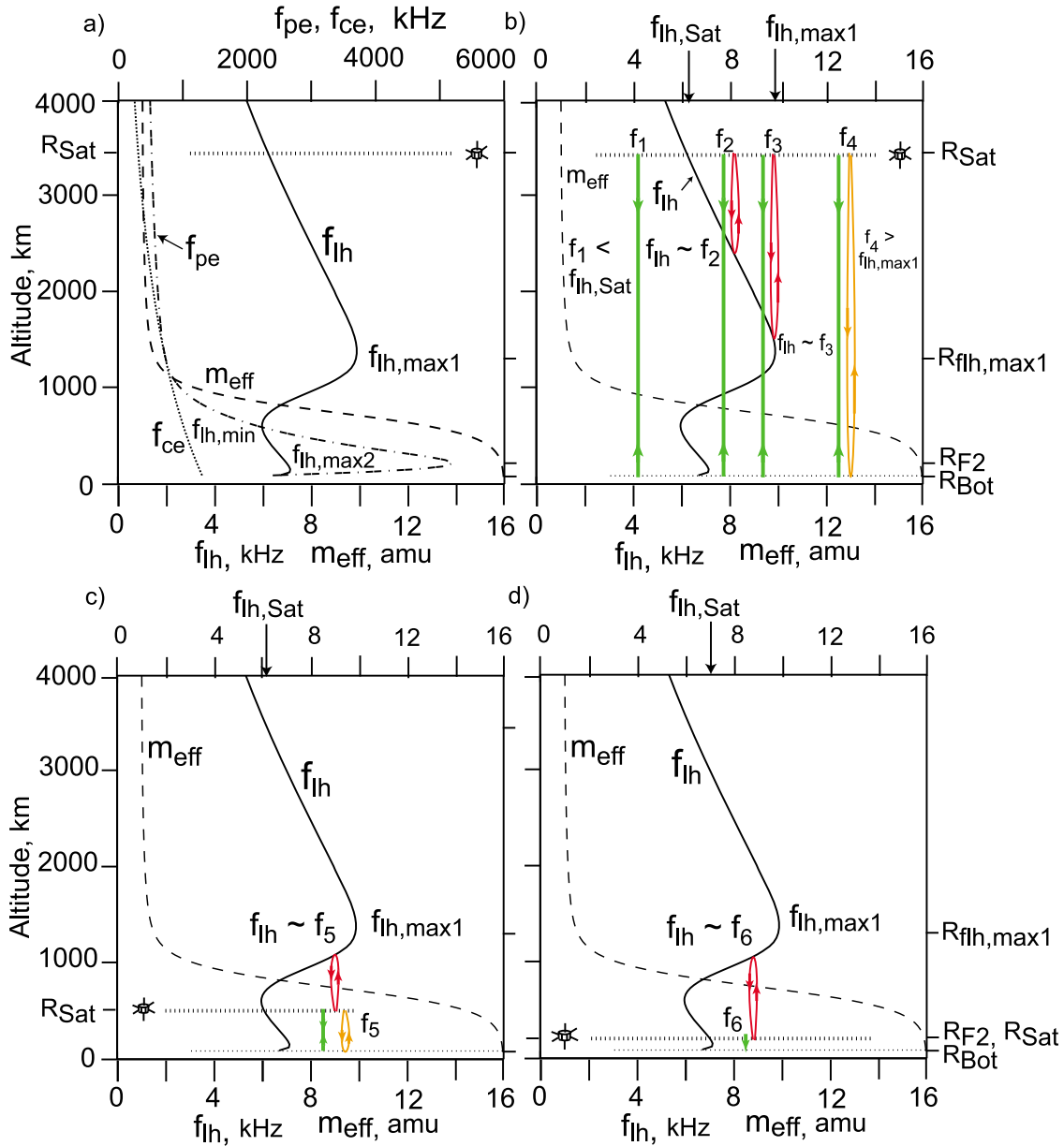


Figure 1. (a) Typical variation of plasma parameters f_{pe} (black dash-dot curve), f_{ce} (black dotted curve), f_{lh} (black solid curve), m_{eff} (black dashed curve), with altitude along the field line passing through the IMAGE satellite. (b) Schematic representation of magnetospheric reflections at altitudes where $f_{lh} \sim f$ (red colored rays) and of specular reflections of normally incident (NI) and obliquely incident (OI) rays at the Earth ionosphere boundary (R_{Bot}) (green and gold colored rays, respectively). (c) Same as Figure 1b but when the sounder is below $R_{flh,max1}$ and near $R_{flh,min}$. (d) Same as Figure 1b but when the satellite is below $R_{flh,max1}$ and near R_{F2} , but above $R_{flh,max2}$, the altitude at which the second maximum in f_{lh} occurs. In this case no OI echo is observed.

$f_{lh,max2} \sim 7$ kHz near (and below) the F2 peak, and then falls monotonically with decreasing altitude to a value $f_{lh,Bot} \sim 6$ kHz at the bottom of the ionosphere. As noted above, the values of various parameters pertinent to the f_{lh} altitude profile are for a specific density model. Our observations and analysis of a large number of WM echoes indicate that these parameters can vary considerably. For example, $f_{lh,max1}$ can vary between 7 and 15 kHz and can occur at $R_{flh,max1} \sim 1000$ – 2000 km. At times $f_{lh,max2}$ can be greater than $f_{lh,max1}$.

[19] The echoing mechanism is a complicated process that depends on the initial wave-normal direction and on changes in the magnitude and topology of the refractive index surface as the wave propagates from the satellite location toward the reflection region. For many initial wave-normal angles, the wave may reflect but not return to the satellite. Paper II discusses in detail how various factors combine to determine what kinds of echoes may be expected for a given magnetospheric plasma model.

[20] In Figures 1b–1d, MR and SR echoes are illustrated for three hypothetical cases, satellite above $R_{f_{lh,max1}}$ (1b), satellite below $R_{f_{lh,max1}}$ and close to $f_{lh,min}$ altitude (1c), and satellite near R_{F2} but above $R_{f_{lh,max2}}$ (1d). When a sounder is above $R_{f_{lh,max1}}$ (1b), possible raypaths for MR echoes (red), NI-SR echoes (green) and OI-SR echoes (gold) are shown for four frequencies $f_1 < f_2 < f_3 < f_4$. For $f_1 < f_{lh,Sat}$, where $f_{lh,Sat}$ is the lower hybrid frequency at the satellite, only NI-SR echoes may be detected; MR echoes are not produced because the topological changes in refractive index that they require are not present along raypaths extending earthward. As discussed in Paper II, most downward raypaths for $f_1 < f_{lh,Sat}$ lead to OI-SR reflections such that the waves propagate away from the L shell of the satellite (because of insufficient ray bending) and thus do not become echoes. For $f_{lh,Sat} < f_2, f_3, < f_{lh,max1}$, MR and NI-SR echoes may both be received according to the wave-normal angles of their propagation (NI-SR for small wave-normal angles and MR for angles near that of the resonance cone). For $f_4 > f_{lh,max1}$, only SR echoes (both NI and OI) would be expected.

[21] As discussed in Paper II, the upper cutoff frequency of the MR echo, $f_{MR,max}$, is close to (within a few hundred Hz of) and lower than $f_{lh,max1}$. The lower cutoff frequency of an OI echo, $f_{OI,min}$, is also close to (within a few hundred Hz of) $f_{lh,max1}$. But, unlike $f_{MR,max}$, depending on the satellite location with respect to $R_{f_{lh,max1}}$, $f_{OI,min}$ may be lower or higher than $f_{lh,max1}$. The following relations hold: $f_{MR,max} \approx f_{lh,max1}$, $f_{MR,max} \approx f_{OI,min}$, and $f_{OI,min} \sim f_{lh,max1}$.

[22] An interesting caustic phenomenon for waves injected at large wave-normal angles is found for frequencies between $f_{MR,max}$ and $f_{OI,min}$, such that no detectable MR or OI echoes are produced. At such frequencies NI echoes at low wave-normal angles are expected. Waves injected at large wave-normal angles undergo either oblique reflection at the ionosphere or MR reflection above $R_{f_{lh,max1}}$, but do not reach the satellite. This caustic phenomenon, the specifics of which depend both on plasma parameters and satellite location, is further discussed in Paper II.

[23] Figure 1c shows that for a sounder operating below $R_{f_{lh,max1}}$ altitude and injecting waves at frequency $f_5 < f_{lh,max1}$, all three types of echoes, MR, NI-SR, and OI-SR could be produced. The MR echo in this case would involve reflection from an altitude above the satellite. If, as shown in Figure 1d, a sounder could operate near the peak of the F layer at R_{F2} and inject at frequency f_6 such that $f_{lh,max2} < f_6 < f_{lh,max1}$, MR and NI-SR echoes could be produced but no OI echoes would be expected (the amount of ray bending in the F region needed for the OI echo would be lacking). The figure also suggests that for a certain range of frequencies between $f_{lh,min}$ and $f_{lh,max2}$, WM waves may remain trapped between the altitudes of $f_{lh,max2}$ and the altitude where $f_{lh} \sim f_{lh,max2}$ above $f_{lh,min}$.

[24] Based on their characteristic spectral forms, WM echoes of all types can be subclassified as discrete, multipath (multicomponent), or diffuse. The discrete spectral forms arise from propagation in a smooth magnetosphere, while those with multicomponent and diffuse spectral forms arise from refraction or scattering due to the presence of FAIs of various scale sizes.

[25] In addition to the MR and SR echoes noted above, there is yet another class of WM echoes that result not from

reflection but from backscattering from FAIs close to the satellite. We classify these as backscattered (BS) echoes. In summary, all three fundamental wave processes, reflection, refraction, and scattering, lead to distinctive echoes.

2.3. WM-Echo Propagation Paths: Effects of FAIs on Echo Propagation

[26] Propagation scenarios for the echoes represented in Figure 1b, extended to include various effects of FAIs and of ducted propagation, are sketched in Figures 2 and 3. Figure 2 focuses on SR echoes, while Figure 3 covers the MR variety. FAIs can be broadly categorized [Sonwalkar, 2006] as small or large scale based on $\lambda_{\perp,IRREG} \ll \lambda$ or $\lambda_{\perp,IRREG} \gg \lambda$, where $\lambda_{\perp,IRREG}$ and λ , respectively, are the irregularity scale size in the direction perpendicular to the field line and the WM wavelength.

[27] Figure 2a shows the propagation path of a discrete NI-SR echo (path A) as well as the looping path of a discrete OI-SR echo (paths B and B'). Because the OI-SR echo path is a loop, it may be traversed in either direction.

[28] Some of the effects of FAIs on SR echoes are indicated in Figures 2b–2d. Figure 2b shows that refraction of SR waves by large (1–10 km) scale irregularities following reflection can lead to propagation along multiple closely spaced paths (B and B'') and hence to the reception of what we call discrete multipath echoes with varying time delays. Such irregularities, located up to several thousand km altitude, have been found to explain multipath propagation of ground transmitter signals to the ISEE-1 satellite [Sonwalkar et al., 1984]. Because these ionospheric irregularities are present almost all the time [e.g., Fejer and Kelley, 1980], discrete echoes almost always show some amount of spreading in time delay at each frequency. Irregularities can also lead to no detection of SR echoes if they affect the raypath (Figure 2b, path B''') of the ray that would have returned to the satellite in the absence of the irregularity.

[29] Figure 2c shows the ducting effect of an irregularity of width 10–100 km. One or more ducts, or field-aligned columns of enhanced or depressed ionization, could be present along or near the field lines passing through the satellite. Unlike ducts required for propagation of lightning whistlers, these ducts need not extend from hemisphere to hemisphere, and may have density enhancements of ~50% or more. Such ducts are frequently present in the highly structured plasma at high latitude [Persoon et al., 1983, 1988] and have been proposed to explain the propagation of impulsive auroral hiss to the ground [Siren, 1975; Sonwalkar and Harikumar, 2000]. Because of the relatively short propagation distances involved, waves with wave-normal angles other than those very close to \mathbf{B}_0 may remain within the duct both before and after reflection. For ducted SR echoes to be seen on IMAGE, it is necessary that the duct extend to low enough altitudes such that whistler mode energy is reflected at the Earth-ionosphere boundary and coupled back into the duct. Examples have been observed on IMAGE and reported by Sonwalkar et al. [2004a]. Some of the reflected energy may return to the satellite along nonducted paths, as in sequences of ducted/nonducted signals reported from the DE-1 satellite [Rastani et al., 1985].

[30] Ducted SR echoes are to be contrasted with the NI-SR echoes shown in Figure 2a. In ducted propagation, the wave-normal direction remains small and the echo raypath

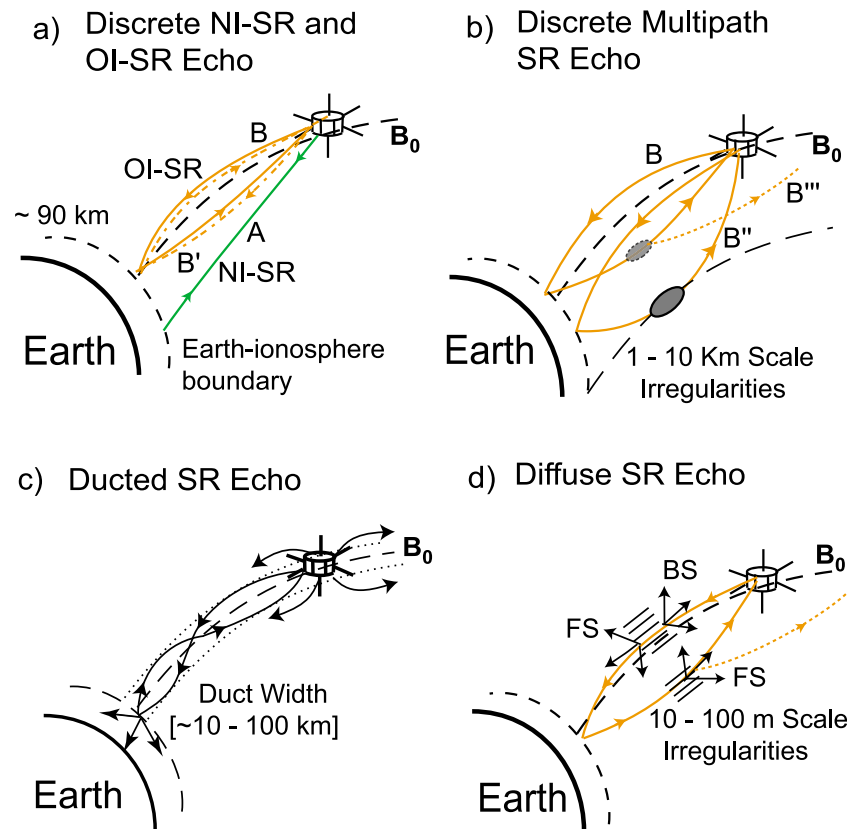


Figure 2. Schematic showing various propagation scenarios that may lead to specularly reflected (SR) whistler mode echoes observed on the IMAGE satellite. (a) Discrete SR echoes due to propagation in a smooth magnetosphere. (b) Discrete multipath SR echoes due to propagation along multiple paths to IMAGE in the presence of large scale irregularities. (c) Discrete SR echoes due to propagation inside a field aligned duct. (d) Diffuse SR echoes due to scattering of signals by small scale (10 m–100 m) irregularities. Adapted from *Sonwalkar et al.* [2004a].

remains close to the field line passing through the satellite. (We do not expect a ducted MR echo, since the wave-normal angle at the reflection altitude for an MR echo would have to be 90°). Meanwhile, in the NI case (Figure 2a), the raypath is not constrained to follow the field line, but instead is dictated by the condition that the wave-normal be normally incident at the earth-ionosphere boundary.

[31] Figure 2d depicts the occurrence of “diffuse” echoes when small scale (10–100 m) field-aligned electron density irregularities are present on the paths of RPI signals from IMAGE. It is known that such FAIs scatter WM waves by linear and nonlinear mechanisms, resulting in spreading of wave-normal angles such that some are close to the resonance cone angle [James, 1978; Bell *et al.*, 1983; Titova *et al.*, 1984; Groves *et al.*, 1988; Bell and Ngo, 1988; Sonwalkar and Harikumar, 2000]. WM waves with different wave-normal angles then reach IMAGE with different time delays, leading to a diffuse appearance on plasmagrams, as shown in section 4. Using the data on lower hybrid waves stimulated by Siple Station VLF transmitter signals and observed on the ISIS-2 satellite, Bell and Ngo [1990] estimated irregularity scale sizes responsible for whistler mode scattering to be ~ 10 –30 m. From the spread of time delays measured in diffuse WM echoes observed on the IMAGE satellite,

Sonwalkar et al. [2004a] estimated the irregularity scale sizes responsible for scattering to be ~ 50 –500 m.

[32] There are two principal ways in which diffuse WM echoes can occur. In one case, signals from RPI incident on small scale FAIs are in part backscattered and in part forward scattered. The forward scattered waves undergo either magnetospheric reflection or specular reflection at the Earth-ionosphere boundary and on the return path are again forward scattered. We call such echoes diffuse MR or SR echoes. Another possibility is that RPI receives only backscattered (BS) signals. This may happen when there are “strongly” scattering FAIs present close to the satellite. We call such echoes BS echoes.

[33] In general the wavelength of the scattered WM waves is comparable to the FAI scale size. For FAIs of the order of 10–100 m scale size the spread in time delays of the received echoes is typically 40 ms or more, compared to the 10–20 ms caused by large FAIs with scale sizes of the order of 1–10 km (as discussed in connection with Figure 2b above and in Paper II).

[34] Figure 3 shows propagation scenarios similar to those of Figure 2, but in this case for MR echoes, Figures 3a–3c represent scenarios for reflection below the satellite and Figures 3d–3f reflection above the satellite.

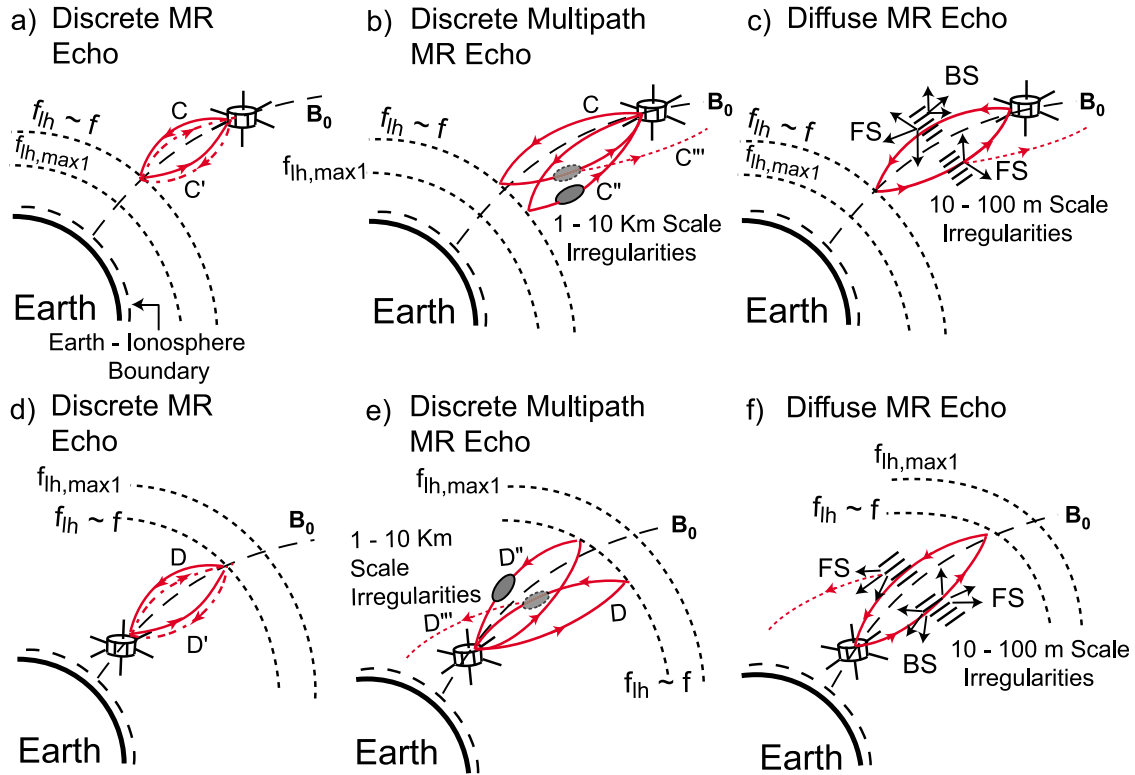


Figure 3. Schematic showing various propagation scenarios that may lead to magnetospherically reflected (MR) whistler mode echoes observed by a sounder operating at an altitude (a–c) above $R_{f_{lh, max1}}$ and (d–f) below $R_{f_{lh, max1}}$. Figures 3a and 3d show discrete MR echoes due to propagation in a smooth magnetosphere. Figures 3b and 3e show discrete multipath MR echoes due to propagation along multiple paths in the presence of large scale irregularities. Figures 3c and 3f show diffuse MR echoes due to scattering of whistler mode signals by small scale irregularities.

[35] In the above discussion of echoes we have assumed that the satellite is located above or below $f_{lh, max1}$ altitude and that $f_{lh, max1} > f_{lh, max2}$ (Figures 1a and 1b). The general features of various WM echoes remain the same when we consider other possibilities such as a satellite location below $f_{lh, min}$ altitude or near F_2 altitude or the condition $f_{lh, max2} > f_{lh, max1}$. There are important differences in certain matters of detail, however. The frequency ranges and initial wave-normal directions of various echoes will depend on values of $f_{lh, min}$, $f_{lh, max2}$, and $f_{lh, max1}$, and on their respective altitudes. Some of the echoes found when the satellite was above the $f_{lh, max1}$ altitude would not be expected had the satellite been below the F_2 peak. For example, no OI-SR would be found for waves injected downward. However, after reflecting at 90 km, some of the associated rays could reach $f_{lh} \sim f$ altitude above the satellite location, undergo magnetospheric reflection there, and thus produce an echo that has undergone a specular and magnetospheric reflection. Such an echo would be similar to the sub-protonospheric (SP) whistler detected on a combination of Alouette satellite, rocket, and ground station records [Carpenter *et al.*, 1964; Smith, 1964]. A full discussion of possible echo generation scenarios based on satellite location and on the relative values and locations of key plasma frequencies is beyond the scope of this paper.

[36] As shown below, IMAGE has observed the principal types of WM echoes that are predicted for a smooth as well

as an irregular magnetosphere. Every type that is predicted for IMAGE at altitudes ranging between ~ 700 km and ~ 5000 km has been found. The lower altitude limit on the observed echoes results from the altitude of the perigee of IMAGE. The upper limit can be explained in terms of experimental limitations such as insufficient radiated power and in particular an insufficient upper limit on measurable time delays.

3. Instrument Description

[37] RPI is a multimode instrument [Reinisch *et al.*, 2000] in which sounding and listening frequencies, range detection, pulse characteristics and repetition rate were adjustable parameters over a wide range of values. The instrument covered the frequency range from 3 kHz to 3 MHz with a receiver bandwidth of 300 Hz. There were three orthogonal thin-wire antennas, two 500-m tip-to-tip dipoles in the spin plane (X and Y) and a 20-m tip-to-tip dipole along the spin axis (Z). The long dipoles were used for transmission, and all three antennas were used for reception. The nominal radiated power from RPI, variable (in terms of free-space-mode excitation) from 0.1 mW at low frequencies to ≈ 10 W per dipole at 200 kHz, was reduced by 3 dB on May 8, 2000 when the power supply for the Y-axis transmitter failed. A further reduction occurred on October 3, 2000, when one of the X-axis monopoles was partially severed, apparently by a

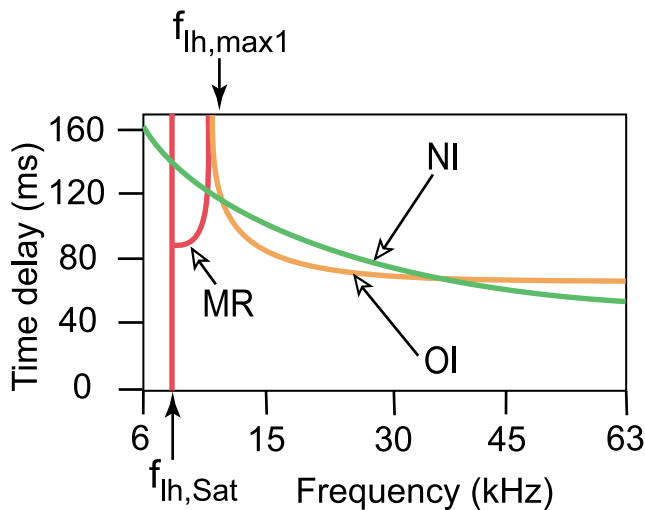


Figure 4. Schematic of time delay (t_g) versus frequency (f) for MR, NI, and OI echoes as they appear on a plasmagram.

micrometeorite, reducing the dipole length to 340 m. On 18 September 2001 an unknown (presumably small and negligible) section of the Y antenna was lost. On 30 September 2004, as a result of an unknown failure of the Y-antenna/receiver system, the signal strength received by the Y-antenna was reduced substantially. The loss of part of the X-antenna and the unknown loss with respect to signal from the Y-antenna has made it difficult to make wave-normal direction measurements [Sonwalkar *et al.*, 2001, 2004b]. On the other hand, as discussed in the next section, the failure of the Y-antenna/receiver system in September 2004 led to an unexpected benefit: it permitted detection of diffuse MR-WM echoes which in a large number of instances could not be recognized on the X and Z antennas because of receiver saturation. In spite of the difficulties with antennas, excellent whistler mode sounding data and passive recordings of background whistler mode waves were acquired over the 5.8 years lifetime of the IMAGE satellite mission, which ended on 18 December, 2005 due to the failure of telemetry.

4. Observations and Interpretation

[38] In the sounding mode, RPI transmitted a sequence of narrow radio pulses of a few ms to a few hundred ms duration in various frequency-time formats within the frequency range 3 kHz - 3 MHz. During typical operations, a sounding program lasting 10–100 s was repeated at intervals of 2–10 min within a schedule containing other programs such as thermal noise (passive recordings) that were used to determine local plasma parameters [Reinisch *et al.*, 2000]. In the first years after launch in 2000 and when operating at low altitude (<5,000–10,000 km) RPI detected a variety of specularly reflected and backscattered whistler mode echoes at all latitudes at frequencies up to 300 kHz [Sonwalkar *et al.*, 2004a]. A new chapter opened with the discovery of MR echoes in the RPI records from January–August 2004 and August–December 2005. During January 2004 to December 2005, IMAGE perigee was in the northern hemisphere, moving from $\Lambda_m \sim 23^\circ\text{N}$ to $\Lambda_m \sim 72^\circ\text{N}$. A special Program (#38) transmitted 3.2 ms pulses in the 6–63 kHz range in

frequency steps of 300 Hz within about one minute. In all, 3.2 ms pulses at 191 distinct frequencies were transmitted. These records also revealed several new features of the specularly reflected and diffuse WM echoes reported earlier [Sonwalkar *et al.*, 2004a] and have helped in their interpretation. Subsequently, another survey of RPI data showed that WM echoes, both MR and SR types, were received during the transmissions of other sounding programs that covered frequency ranges of potential interest.

[39] Figure 4 provides in typical plasmagram coordinates of travel time in milliseconds versus sounder frequency, a sketch of the principal echo phenomena to be discussed below, including the MR echo, the OI-SR and NI-SR echoes, and a plasma resonance (lower hybrid resonance labeled $f_{lh,Sat}$) at the low frequency edge of the MR echo (because of the slow-wave nature of whistler mode propagation, travel time is displayed instead of the otherwise typical free space echo range). Also shown are representative values of the frequency range in which the echoes have been observed. Key features of the MR echo shown in the figure include a lower cutoff at $f_{lh,Sat}$, an upper cutoff near $f_{lh,max1}$, and dispersion in which time delay typically increases with frequency. The key features of the SR echoes shown in the figure include a lower cutoff for OI-SR near $f_{lh,max1}$, no lower cutoff for NI-SR, and characteristic dispersion in which time delay typically decreases with frequency. The relative values of the time delays of the three echoes are found to vary depending upon the location of the satellite and the transmission frequency range. In the above discussion we have assumed that the satellite is located above $f_{lh,max1}$ altitude and the transmission frequency range covered is 6 to 63 kHz.

4.1. Illustrative Examples of Whistler Mode Echoes

4.1.1. Examples of WM Echoes for IMAGE Altitude Above $R_{f_{lh,max1}}$: MR and OI Echoes

[40] Figures 5a and 5b show plasmagrams of magnetospherically reflected (MR) echoes and obliquely incident specularly reflected (OI-SR) echoes received by the X-antenna on RPI/IMAGE on 22 and 26 October 2005, respectively. For brevity we refer to the entire set of echoes appearing as a single trace within a range of frequencies on a plasmagram as either an MR or an SR echo.

[41] The echoes shown in Figure 5a were observed well inside the plasmasphere as determined from plasma density measurements along the associated orbit (plasmopause at $L = 5.5$ dayside, $L = 4.5$ nightside). The IMAGE location was given by $R = 1.53 R_E$ (altitude = 3404 km), $\lambda_m = 31.9^\circ\text{N}$, $L = 2.13$, and $MLT = 11.2$.

[42] The altitude indicates that IMAGE was above $R_{f_{lh,max1}}$ (see Figure 1b). The MR echo in Figure 5a had a lower cutoff $f_{MR,min} = 6.3$ kHz, an upper cutoff $f_{MR,max} = 9.3$ kHz, and the time delay increased with frequency from an apparent minimum at ~ 90 ms. A plasma resonance, a narrow vertical trace (indicated by an arrow below the plasmagram), appeared at the lower frequency cutoff. This frequency was identified as $f_{lh,Sat}$, the lower hybrid resonance at the satellite (see section 2). The lowest-frequency part of such echoes usually occupied one to two frequency bins (0.3 or 0.6 kHz). The upper cutoff $f_{MR,max}$ was close to (within ~ 1 kHz of), the maximum lower hybrid frequency $f_{lh,max1}$ along the field line passing through the satellite (see Paper II). The echo at

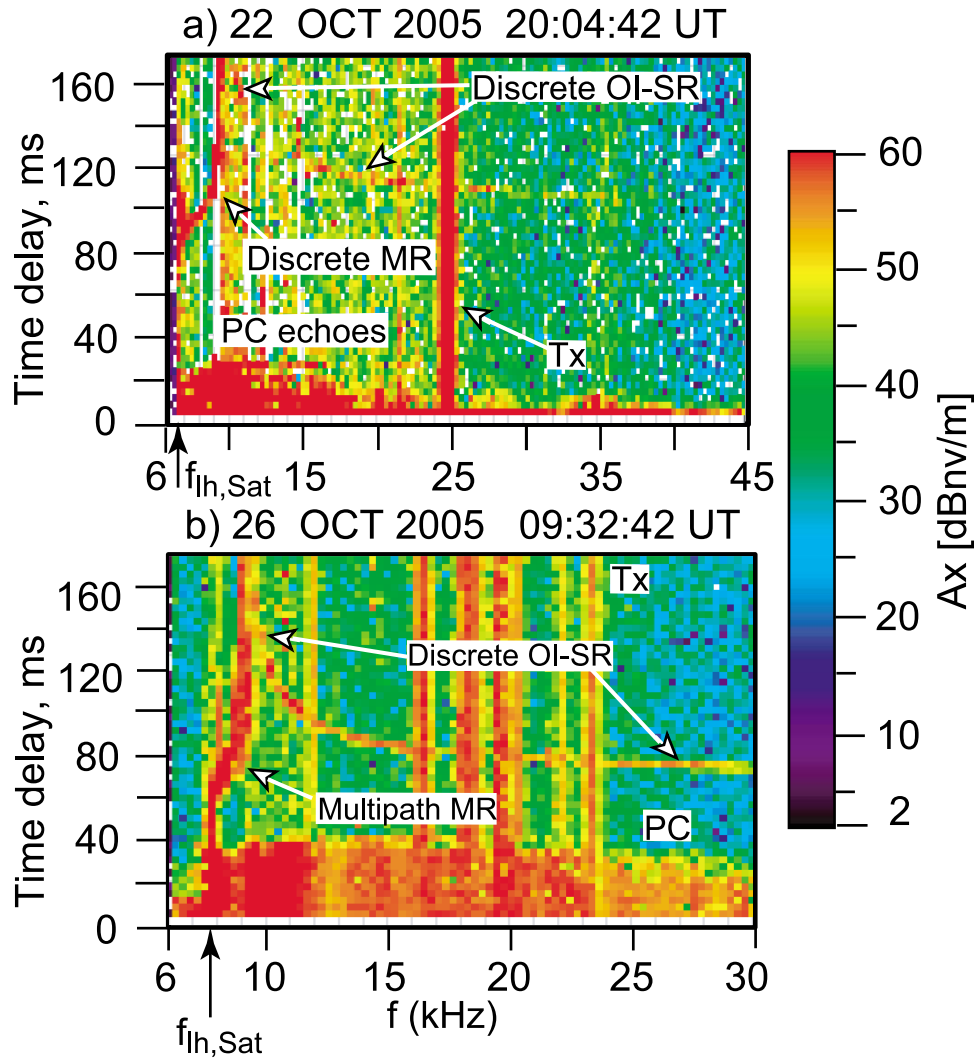


Figure 5. Examples of magnetospherically reflected (MR) and obliquely incident specularly reflected (OI-SR) whistler mode echoes received during the transmission of Program #38. (a) Discrete MR and discrete OI echoes observed when the satellite was at ~ 3400 km altitude, above $R_{f_{lh,max1}}$. (b) Multipath MR and discrete OI echoes observed when the satellite was at ~ 2600 km altitude, above $R_{f_{lh,max1}}$.

the upper cutoff generally occupied one frequency bin (0.3 kHz).

[43] The propagation scenario of the MR echoes shown in 5a is illustrated by red raypaths at f_2 and f_3 in Figure 1b and by the (red) raypath C or C' in Figure 3a. In the case of Figure 5a the SR echoes appeared above ~ 10 kHz. They exhibited a group time delay that decreased with frequency, curving downward from a lower cutoff frequency $f_{OI,min} = 10.2$ kHz $> f_{MR,max}$. Because of this low frequency cutoff we believe that the SR echoes were the obliquely incident (OI) variety (gold ray at f_4 in Figure 1b and rays B and B' in Figure 2a). Note that the OI echo was observed at frequencies ranging from 10.2 to 11.4 kHz, 14.4 to 14.7 kHz and 15.9 to 33.3 kHz. The conspicuous gaps between 11.4 and 14.4 kHz and between 14.7 and 15.9 kHz may be attributed to deflection of the raypaths at these frequencies due to the presence of FAIs (Figure 2b, path B'''). We call such echoes containing gaps as patchy echoes. The plasma frequency f_{pe} , estimated from passive recordings of the upper hybrid frequency $f_{uh} \approx$

666 kHz, and the model $f_{ce} \approx 321$ kHz was 584 kHz [Benson et al., 2004]. Both the MR and OI-SR echoes were observed at frequencies well below local f_{pe} and f_{ce} , confirming the whistler mode character of their propagation. Assuming $m_{eff} = 1$, a good assumption at 3403 km altitude, we can estimate from equation (1) that f_{lh} was ~ 6.3 kHz, consistent with our earlier statement that the lower cutoff of the MR echo is the local lower hybrid frequency.

[44] The echoes shown in Figure 5b were observed when IMAGE was at $R = 1.40 R_E$ (altitude = 2574 km), $\lambda_m = 38.8^\circ N$, $L = 2.31$, and MLT = 12.1. In this case the satellite was again above the $R_{f_{lh,max1}}$ altitude. The model f_{ce} was 454 kHz, measured f_{uh} was 705 kHz, and the estimated f_{pe} was 539 kHz. The estimated lower hybrid frequency (assuming $m_{eff} = 1$) using (1) was 7.8 kHz. The MR echo had a lower cutoff at 7.8 kHz, again equal to the estimated f_{lh} at the satellite, and an upper cutoff at 9.3 kHz. The echo time delay increased with frequency from an apparent minimum of ~ 65 ms. There was time delay spreading that varied from 20 ms to

80 ms, believed to be the result of the refraction or scattering by large and small scale FAIs suggested in Figures 3b and 3c. The accompanying OI-SR echo had a lower cutoff at 9.9 kHz. It showed relatively small, 3–6 ms, spreading in time delay, indicating that its propagation path, rays B and B' in Figure 2a, lay in a relatively smooth part of the magnetosphere.

[45] The difference in time delay spreading between the MR (20–80 ms) and OI-SR (3–6 ms) echoes can be explained in terms of the different regions that their paths covered. The regions could be different either because: (1) the ray propagation paths were different for different frequencies and wave-normal angles, or (2) the different frequencies were transmitted at different times. In the specific example of Figure 5b, the propagation paths were almost along the field line passing through the satellite for both MR and OI-SR echoes (see Paper II ray tracing simulations). Thus the main contributing factor is believed to have been satellite motion. For Program #38, the satellite moved about 30 km ($\Delta L \sim 0.006$) in the ~ 4 seconds needed to transmit pulses in the frequency range 6–10 kHz. Thus it is possible that small scale (~ 10 – 100 m) FAIs were present along the field lines passing through IMAGE during transmission of the 6–10 kHz part of the program and later were not present during transmission of the higher frequencies. The time delay spread of the MR echoes was itself highly variable, indicating that small scale FAIs can be highly structured over the spatial scale of 30 km and/or that their structure affects various frequencies differently. Overall, this example suggests that WM sounding could provide a sensitive method of investigating the presence of plasma structure along geomagnetic field lines.

[46] As shown in Figures 1b and 2a, we expect to observe both OI-SR and NI-SR echoes when the satellite is above $R_{f_{ih,max1}}$ altitude. OI echoes are predicted for frequencies above $f_{ih,max1}$ with lower cutoff near $f_{ih,max1}$ and with time delay decreasing with frequency. In contrast, NI echoes are predicted at all frequencies (no low frequency cutoff near $f_{ih,max1}$) with time delay decreasing with frequency. Thus it should be easy to distinguish OI and NI echoes if they occur at frequencies near $f_{ih,max1}$. As discussed in Paper II, OI and NI echoes may be distinguished at higher frequencies based on the slope of their dispersion curves of travel time t_g versus f .

[47] Horizontal traces below about 40 ms time delay in Figure 5 represent proton cyclotron (PC) echoes [Carpenter *et al.*, 2007]. PC echoes almost always accompanied MR echoes, but the converse was not true.

[48] In Figure 5, the vertical traces above 10 kHz covering the entire time axis range are ground transmitter signals (Tx), in 5a clearly visible at ~ 25 kHz; in 5b at 11.7–12.0, 16.2–16.8, 18–18.6, 19.5–20.4, 22.2, and 23.1–23.7 kHz. There being many VLF transmitters on Earth, signals from these were regularly found on RPI plasmagrams. Though most ground transmitter signals have a nominal bandwidth of a few hundred Hz, these signals often occupied several 300-Hz frequency bins on plasmagrams. This apparent spectral broadening, sometimes by as much as 2 kHz, can be explained by scattering of ground transmitter signals by small scale FAIs [Bell *et al.*, 1983]. Another possibility is that because of the slow roll-off of the receiver filter and

variations in signal amplitude, the signal could at times occupy more than one frequency bin.

4.1.2. Examples of WM Echoes for IMAGE Altitude Above $R_{f_{ih,max1}}$: MR and NI Echoes

[49] Plasmagrams in Figures 5a and 5b clearly show OI echoes but no evidence of NI echoes. It is possible that in most of the soundings from above $R_{f_{ih,max1}}$, the RPI antenna did not generate sufficient WM radiation at the low wave-normal angles and the low frequencies required for the generation of NI echoes close to $f_{ih,max1}$. Another possibility is that low wave-normal WM waves injected from IMAGE encountered FAIs which deflected their raypaths. As indicated in Figure 2a, the raypath of an NI echo tends to deviate from the field line \mathbf{B}_0 passing through the satellite, whereas the paths of MR and OI lie close to \mathbf{B}_0 . Thus it is possible that in some cases WM waves injected at small wave-normal angles that were capable of producing NI echoes encountered FAIs, whereas those injected at large wave-normal angles and producing MR and OI echoes did not. When NI echoes were evident, they were generally found at higher frequencies and from sounder altitudes below $R_{f_{ih,max1}}$.

[50] We did find one example of an NI echo at frequencies below $f_{ih,max1}$, illustrated in Figure 6 when IMAGE was at 2440 km, $\lambda_m = 28.5^\circ\text{N}$, $L = 1.79$, $\text{MLT} = 8.0$, model $f_{ce} = 514.4$ kHz. Figure 6a, from the X antenna, shows a diffuse MR echo and a discrete NI echo that extends below 8 kHz, the low frequency limit of the MR trace. In Figure 6a the lower and upper cut off frequencies of the MR echoes cannot be identified. Often diffuse MR echoes were better identified on the Y-antenna (see explanation below in section 4.3 of the special use of the damaged Y antenna to distinguish echo features). Figure 6b, from the Y antenna, shows a discrete MR echo, presumably embedded in the diffuse band shown in Figure 6a. In Figure 6b, SR echo is barely visible. In this figure, two SR echo segments that appear stronger than the background in the ranges 7.5–8.1 kHz and between 44.7–50.1 kHz have been identified by comparing the plasmagram of Figure 6b with that of Figure 6a. As shown in section 4.3, in general it is easier to identify various types of WM echoes by comparing plasmagrams from the X-, Y-, and Z-antennas. In order to further verify this particular identification of MR and NI-SR echoes, we performed ray tracing analysis and found that for a reasonable magnetospheric density model it is possible to match the calculated time delays with those observed.

4.1.3. Examples of WM Echoes for IMAGE Altitudes Below $R_{f_{ih,max1}}$

[51] Over the 5.8 years of IMAGE operation (March 2000 – December 2005), perigee altitude varied between ~ 600 and ~ 1600 km. In early 2004 perigee was near its lowest altitude, ~ 600 km, permitting observations of MR echoes when IMAGE was most likely below the $f_{ih,max1}$ altitude.

[52] Figures 7a and 7b show multipath MR echoes observed on 23 Jan 2004 (altitude = 715 km, $\lambda_m = 39.2^\circ\text{N}$, $L = 1.85$, $\text{MLT} = 17.1$) and 11 Mar 2004 (altitude = 819 km, $\lambda_m = 30.4^\circ\text{N}$, $L = 1.52$, $\text{MLT} = 13.7$), respectively. In Figure 7a we have $f_{MR,min} = 6.3$ kHz and $f_{MR,max} = 8.7$ kHz and in Figure 7b $f_{MR,min} = 9.6$ kHz and $f_{MR,max} = 11.4$ kHz. Unlike MR echoes observed when IMAGE was above $f_{ih,max1}$ altitude, these echoes were not accompanied by a pronounced f_{ih} resonance, typically indicated by a vertical trace covering the entire time delay axis (e.g., Figures 5a and 5b).

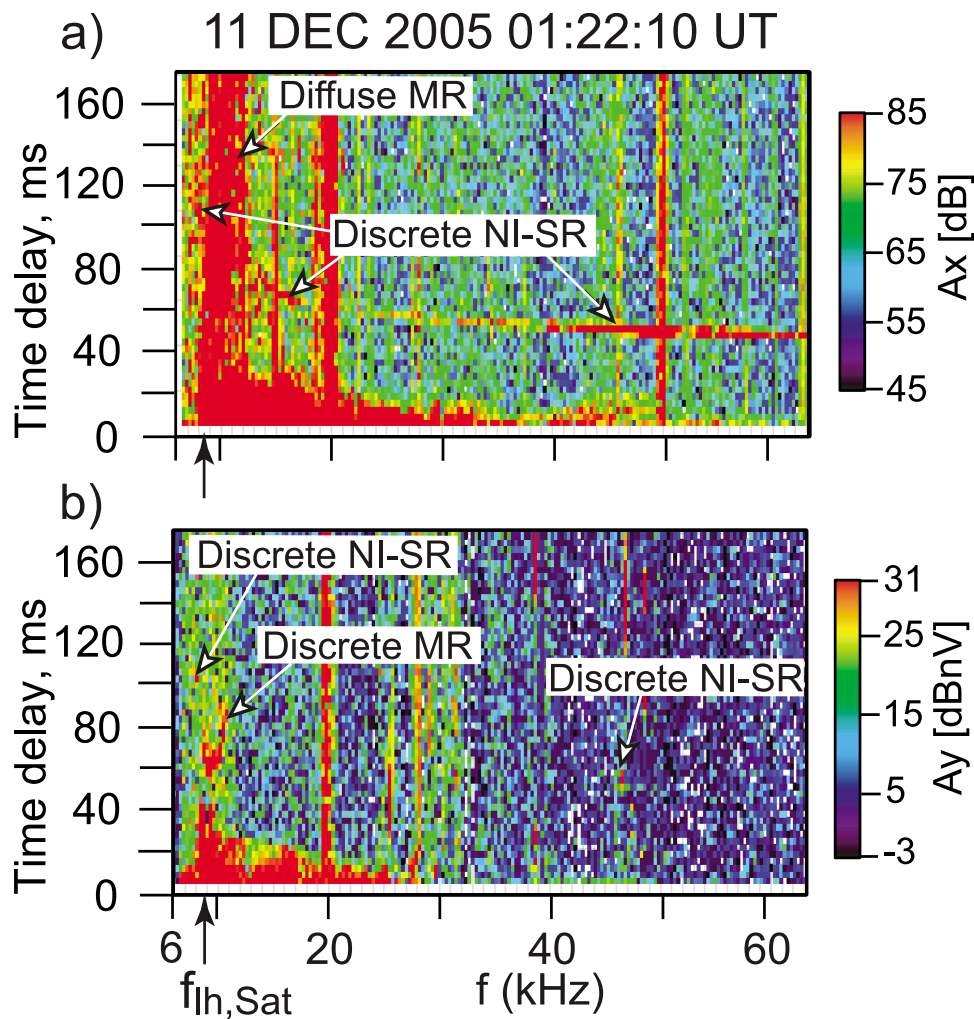


Figure 6. Examples of magnetospherically reflected (MR) and normally incident specularly reflected (NI-SR) echoes received during the transmission of Program #38. (a) Diffuse MR and discrete NI echoes observed on the X-antenna when the satellite was at 2440 km altitude, above $R_{f_{lh,max1}}$. (b) The same echoes as in Figure 6a but observed on the Y-antenna, clearly showing the MR echo with a minimum in time delay and portions of discrete NI echoes (see text for details).

The time delays at frequencies 300 Hz above the lower echo cutoffs of ~ 6.3 and ~ 9.6 kHz were near 30 ms, much shorter than the >60 –80 ms typically observed at those frequencies for cases like those in Figures 5a and 5b.

[53] Both echoes in Figure 7 showed evidence of multipath as indicated by a ~ 10 –20 ms time delay spread at each frequency. These echoes were not accompanied by SR echoes. If we compare the frequency ranges of these MR echoes with the f_{lh} versus altitude plot in Figure 1b, it appears likely that they resulted from the reflection of RPI signals from the bottomside of the f_{lh} curve just below the $f_{lh,max1}$ altitude. If so, then on 23 Jan and 11 Mar 2004 $f_{lh,max1}$ was roughly 8.7 and 11.4 kHz, respectively. The raypaths of the echoes are suggested by the red raypath for frequency f_5 in Figure 1c and by the paths D and D' in Figure 3e.

[54] Figure 8a shows examples of MR, NI-SR, and OI-SR echoes observed on 21 June 2004 (altitude = 1280 km, $\lambda_m = 62.4^\circ\text{N}$, $L = 5.58$, $\text{MLT} = 6.3$). The MR echoes were observed at the adjacent sounding frequencies of 6.6, 6.9,

and 7.2 kHz as shown on the expanded plasmagram of Figure 8b. Although data were missing at 6.0 and 6.3 kHz, it is likely that MR echoes reached IMAGE at these frequencies and below. Despite background noise, NI-SR and OI-SR echoes are visible in the ranges ~ 34 –52 kHz and ~ 22 –41 kHz, respectively (8a). In the data surveyed so far, we have found only one other example, from 01 Feb 2003, in which all three basic types of echoes were detected. Satellite altitude in this case was not low enough to unambiguously indicate a position below $R_{f_{lh,max1}}$. However, ray tracing simulations, assuming for this case a model magnetosphere with $R_{f_{lh,max1}} \sim 2100$ km, showed agreement between the measured and calculated time delays for MR, NI-SR, and OI-SR echoes over the observed frequency range, suggesting that IMAGE was indeed below the $R_{f_{lh,max1}}$ altitude.

[55] A band of noise around ~ 10 kHz with a bandwidth of ~ 2 –5 kHz was frequently seen on plasmagrams. It appears in Figures 8a and 8b in the frequency range 8 to 12.5 kHz. The origins of this noise are not clear.

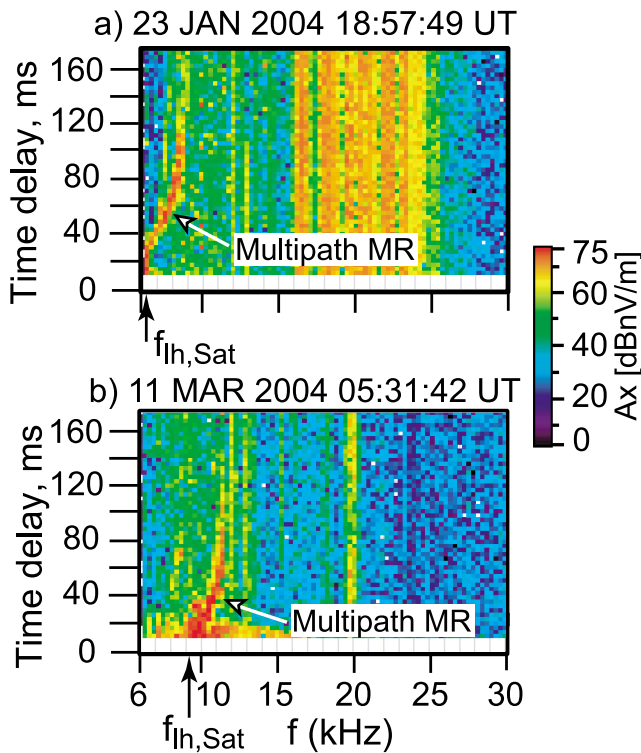


Figure 7. MR echoes observed at sounder altitudes below the level where $f_{lh} = f_{lh,max1}$. (a) Multipath MR echo observed on 23 January 2004. (b) Multipath MR echo observed on 11 March 2004.

[56] In 2004 when IMAGE was at low altitude near perigee, many examples of NI-SR and OI-SR echoes were found, typically at frequencies greater than ~ 50 – 100 kHz, with both types often on the same plasmagram. These echoes occurred during the transmission of Program #57, which consisted of 3.2-ms pulses in the 20 to 326 kHz frequency range with 1.2 kHz linear stepping. Figure 9 shows examples of SR echoes observed on 01 July 2004 (altitude = 1337 km, $\lambda_m = 7.1^\circ N$, $L = 1.23$, $MLT = 6.8$) and 14 July 2004 (altitude = 1152 km, $\lambda_m = 16.6^\circ N$, $L = 1.29$, $MLT = 5.9$). Figure 9a shows simultaneously occurring OI-SR and NI-SR echoes, both reflecting from the Earth-ionosphere boundary in the northern hemisphere. Figure 9b shows examples of NI-SR echoes that reflected from both the local hemisphere (northern) and the conjugate southern hemisphere. Because the lower frequency part of these echoes was buried in a strong noise background, possibly of natural origins, ray tracing analysis was carried out to confirm these interpretations. The ray tracing analysis also indicated that in both cases IMAGE was below the $R_{f_{lh,max1}}$ altitude.

4.2. Influence of Field Aligned Irregularities on WM Echoes

4.2.1. Discrete, Multipath, and Diffuse MR Echoes: Forward-Scattered and Backscattered MR Echoes

[57] Figures 10a–10e illustrate features of MR echoes received within the plasmasphere. Records 10a, 10b, 10c, and 10d show the echo amplitude observed on the X-antenna, whereas 10e shows the net amplitude on three antennas.

Figure 10f shows the locations of IMAGE in the magnetic meridional plane where the echoes were observed. A reference orbit for 16 November 2005 is indicated. Based on the IMAGE altitude (>2000 km) we believe that all the MR echoes in Figure 10 were produced by reflections occurring below the satellite altitude. As in the cases of Figure 5, these echoes exhibited minimum and maximum frequency cutoffs and a generally increasing time delay with frequency, while differing from one another in their dispersion characteristics.

[58] The MR echo in Figure 10a showed a broad minimum in time delay near 8 kHz, whereas those in 10b and 10c did not. Such a minimum in time delay was generally observed during sounding from the higher altitudes (>3000 km). As expected from Figure 1, the lower cutoff frequency $f \simeq f_{lh,Sat}$ increased with decreasing altitude (compare 10a with 10b and 10c). The time delays at the lower cutoff covered the entire time delay axis range. We interpret this as the result of excitation of $f_{lh,Sat}$, the local lower hybrid resonance.

[59] In Figure 10a, the time delays at each MR echo frequency (except for the lower and upper cutoff frequencies) occupied one or two range bins (3–6 ms), while the delays for the MR in Figure 10b occupied 3 to 6 bins or more (10–20 ms or more) and those for the echoes in 10c occupied ~ 100 ms. The echoes in Figure 10b are called multipath MR echoes, probably produced by the mechanism shown in

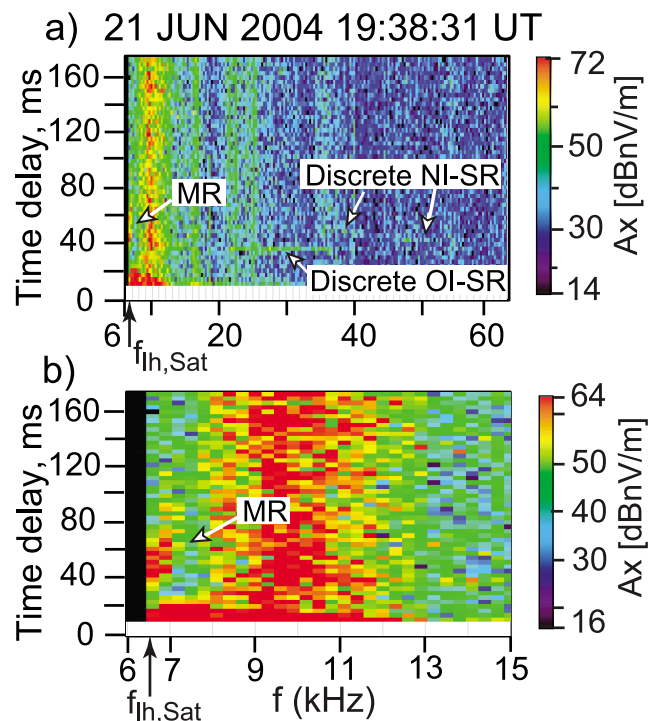


Figure 8. Examples of magnetospherically reflected (MR), normally incident (NI), and obliquely incident (OI) specularly reflected (SR) echoes received during sounding by RPI on 21 June 2004 from altitudes below $R_{f_{lh,max1}}$. (a) Discrete NI-SR, discrete OI-SR and multipath MR echoes observed during the transmission of Program #38. (b) Expanded version of plasmagram (Figure 8a) to show the multipath MR echoes at 6.6, 6.9, and 7.2 kHz.

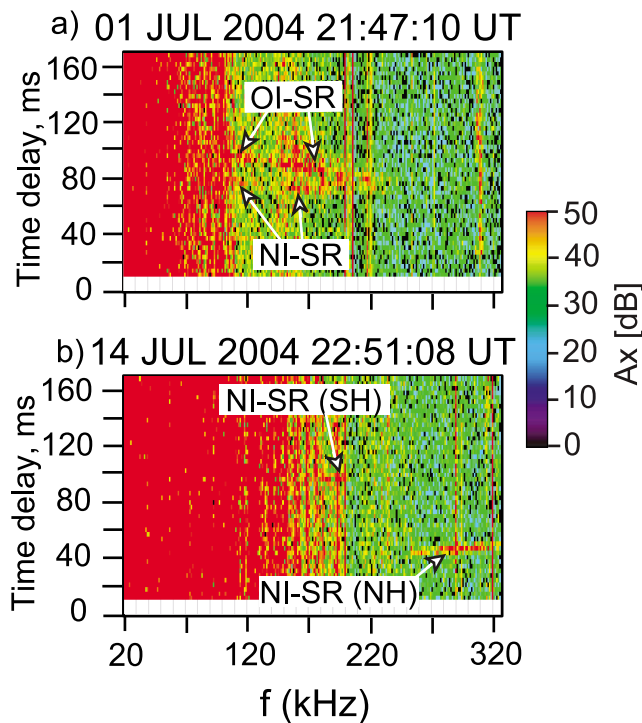


Figure 9. Examples of specularly reflected (SR) echoes received by RPI in 2004 during radio soundings using Program #57 at altitudes below $R_{plh,max1}$. (a) Multipath NI-SR and OI-SR echoes observed on 1 July 2004. (b) Discrete NI-SR echo reflected from the northern hemisphere (NH) and discrete NI-SR echo reflected from the southern (conjugate) hemisphere (SH) observed on 14 July 2004.

Figure 3b. Those in 10c and 10d are called diffuse MR echoes and were probably produced by the mechanism shown in Figure 3c. Figure 10c is considered an example of the forward scattered diffuse MR echo. The well defined boundary is the signature of the lowest time delays of the MR echo that would propagate in a smooth magnetosphere. The diffuseness at higher time delays occurred because of the forward scattering of the RPI signal after undergoing MR reflection. It is possible that the FAIs responsible for forward scattering on the return leg also caused such scattering on the downgoing leg. However, the sharp boundary of the MR echo suggests that any forward scattered downgoing components did not survive Landau damping (see Paper II for further discussion of Landau damping and hot plasma effects on whistler mode propagation).

[60] Compared to the echoes shown in 10a-c, the MR echo in Figure 10d has unusual dispersion characteristics. It does not show a well defined $t_g - f$ trace as in Figures 10a–10c, and the time delay at each frequency ranges from ~ 6.4 ms, the shortest possible for a 3.2 ms pulse, to 175 ms, the longest allowed by Program #38. We believe that this echo was a result of both backscattering by FAIs very close to IMAGE, leading to the shorter time delays, and forward scattering leading to the longer time delays. Diffuse echoes such as the one shown in Figure 10d show clear evidence of the MR echo phenomenon when seen on the plasmagram

obtained from the Y-antenna (see section 4.3). Auxiliary material shows the MR echo of Figure 10d as observed on X-, Y-, and Z-antennas.¹

[61] Figure 10e shows an example of echoes in which the lower frequency transmissions (~ 8.7 – 12.0 kHz) led to diffuse MR echoes with time delays ranging from 100 ms to 170 ms and the higher frequency transmissions (~ 12.0 – 14.1 kHz) to discrete MR echoes (this upper frequency of 14.1 kHz is one of the highest we have measured). A possible explanation is that the field lines covered by the echo raypaths at the lower frequencies contained small scale FAIs and those covered by the echoes at higher frequencies lay in a smooth magnetosphere. Assuming a satellite velocity of ~ 8 km/s, the latitudinal distance covered by IMAGE during the transmissions of 8.7 kHz to 12.0 kHz (~ 3 s) was ~ 25 km and during the transmissions of 12.0 to 14.1 kHz (~ 2 s) was ~ 16 km. Both distances were thus much greater than the scale size ~ 10 to 100 m of small scale FAIs, consistent with our assumption that the transmitted RPI signals encountered FAIs during the transmissions of 8.7 to 12 kHz signals and did not do so during the transmissions of 12 to 14.1 kHz signals.

[62] As indicated by arrows, the MR echoes shown in Figures 10b–10d were accompanied by discrete SR echoes. Although not so indicated in the figure, the SR echoes shown in Figure 10d extended up to 63 kHz, as did the one shown in Figure 6a.

4.2.2. Discrete, Multipath, and Diffuse SR Echoes: Forward-Scattered SR and Backscattered Echoes

[63] Program #38 has revealed new features of SR echoes not noticed earlier:

[64] (1) Two types of discrete SR echoes can be produced, one with small initial wave-normal angle ($\theta_i < \theta_G$, where θ_G is the Gendrin angle) and one with large initial wave-normal angle ($\theta_i > \theta_G$).

[65] (2) Two types of diffuse SR echo may be observed, one that has undergone specular reflection at the bottom of the ionosphere as well as scattering by FAIs, and one that has undergone backscattering of the RPI signal by small scale FAIs close to the satellite. In work by *Sonwalkar et al.* [2004a], only the backscattered diffuse echoes were identified.

[66] Figures 11a–11c show, respectively, examples of discrete, multipath, and diffuse SR echoes. In Figure 11a a “discrete” SR echo appears above ~ 9 kHz, similar to the ones shown in Figures 5a and 5b above ~ 10 kHz. Echoes such as these result from RPI signals propagating in a relatively smooth magnetosphere, as in the scenario of Figure 2a [*Sonwalkar et al.*, 2004a]. They are believed to propagate downward in the nonducted mode, such that wave-normal direction makes a nonzero angle with respect to \mathbf{B}_0 .

[67] Figure 11b shows an example of an SR echo with a time delay spread of 3–6 ms at frequencies below 30 kHz and above 55 kHz and a spread of 10–20 ms between 30 and 55 kHz. The echoes below 30 kHz are attributed to propagation in a smooth magnetosphere, while those at frequencies between 30 and 55 kHz are believed to result from propagation downward in a region containing 1–10 km scale irregularities, reflection at the Earth-ionosphere boundary,

¹Auxiliary materials are available in the HTML. doi:10.1029/2011JA016759.

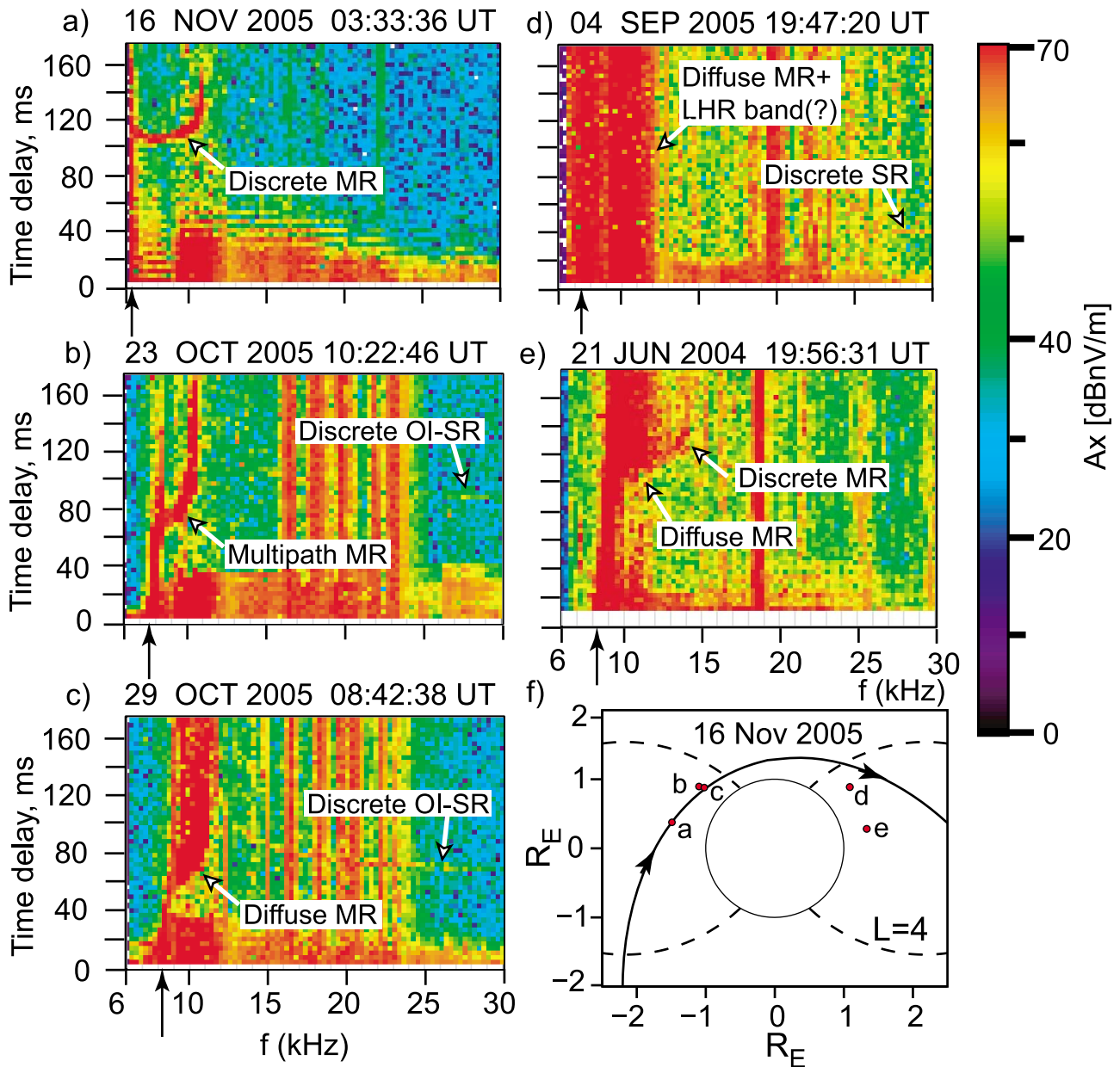


Figure 10. RPI plasmagrams illustrating various features of MR echoes seen on the IMAGE satellite. The arrows on the frequency axes indicate the lower cutoffs $f_{\min,MR} \sim f_{lh,Sat}$ of MR echoes. (a) Discrete MR echo showing a broad minimum in time delay (altitude = 3421 km, $\lambda_m = 14.3^\circ\text{N}$, $L = 1.64$, $\text{MLT} = 10.0$). (b) Discrete multipath MR echo (2654 km, $\lambda_m = 39.24^\circ\text{N}$, $L = 2.36$, $\text{MLT} = 12.3$). (c) Diffuse MR echo (2490 km, $\lambda_m = 38.52^\circ\text{N}$, $L = 2.27$, $\text{MLT} = 11.9$). (d) Diffuse MR echoes with time delay covering the entire range of the time delay axis (4–170 ms) (2576 km, $\lambda_m = 40.73^\circ\text{N}$, $L = 2.45$, $\text{MLT} = 2.5$). (e) Diffuse (8.7–12.0 kHz) and discrete (12.0–14.1 kHz) MR echoes observed during a single transmission of Program #38 (2279 km, $\lambda_m = 12.36^\circ\text{N}$, $L = 1.42$, $\text{MLT} = 1.4$). (f) Plot of the low-altitude portion of the IMAGE polar orbit for the case of Figure 10a. The approximate locations of IMAGE in the magnetic meridional plane for the five cases are indicated by red dots. Dipole field lines at $L = 4$ are shown as a reference.

and return to the satellite via multiple paths, as illustrated by paths B and B' in Figure 2b.

[68] We often observe a discrete SR echo (not shown) similar to the one shown in Figure 5a, but with a more gradually sloping $t_g - f$ curve. In such cases, the signal propagates along a raypath close to the geomagnetic field line because of the presence of FAIs of scale sizes ~ 10 – 100 km,

generally called ducts. The wave-normal direction remains close to \mathbf{B}_0 . Ducted and nonducted echoes can be distinguished by their differing $t_g - f$ characteristics.

[69] When sounding over mid-to-high latitudes, RPI has observed strong echoes with time delays spread well beyond those observed in “discrete” or multipath SR echoes. Figure 11c provides an example of what are called diffuse

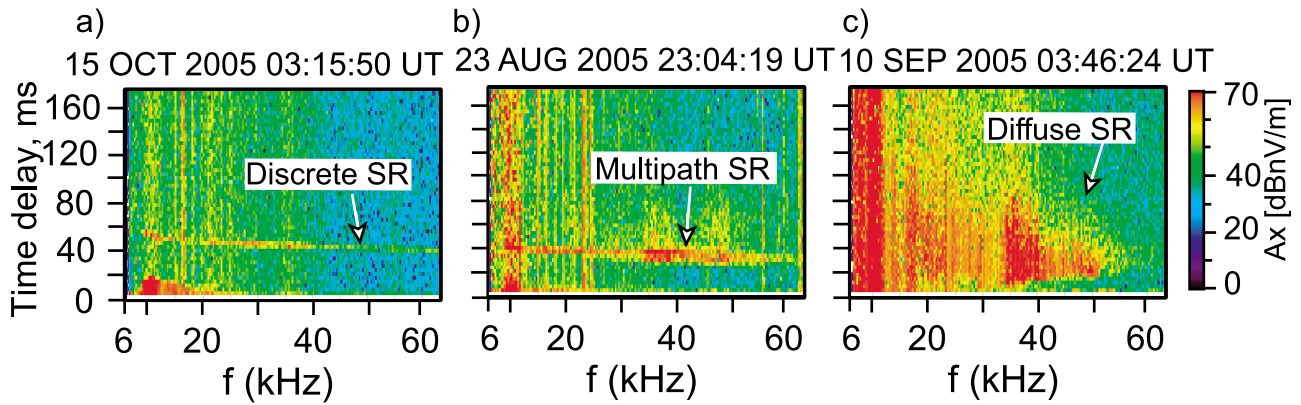


Figure 11. Plasmagrams showing examples of the variety of spectral forms of SR echoes received during soundings by RPI. (a) Discrete SR echoes observed on 15 October 2005, (1776 km, $\lambda_m = 56^\circ\text{N}$, $L = 4.14$, $\text{MLT} = 11.7$) resulting from propagation in a smooth magnetosphere. (b) Discrete multipath echoes observed on 23 August 2005 (1915 km, $\lambda_m = 59.7^\circ\text{N}$, $L = 5.1$, $\text{MLT} = 4.16$), possibly resulting from refraction of RPI signals by large scale irregularities. There is also evidence of diffuse forward scattered SR echoes between 32 and 50 kHz. (c) Diffuse SR echoes observed on 10 September 2005 (1855 km, $\lambda_m = 76.91^\circ\text{N}$, $\text{MLT} = 4.3$), possibly the result of scattering by small scale irregularities.

echoes, typically received at low altitudes (<5000 km) outside the plasmopause and over auroral and polar regions. In contrast to the traces of Figures 11a and 11b, in which time delay spreading at each frequency varied from 3 to 30 ms, here the time delays were spread over as much as 60 ms at frequencies between 12 kHz and 60 kHz, with the most pronounced spreading at the lower frequencies. We believe that in this case the signal was scattered (Figure 2d) by small scale (10 m–100 m) FAIs, commonly observed in the magnetosphere up to several-thousand km altitude. It has been shown that WM signals can be strongly scattered by both linear and nonlinear mechanisms [James, 1978; Bell and Ngo, 1988; Titova et al., 1984; Groves et al., 1988] into quasi-electrostatic waves with wavelengths of the same order of magnitude as the spatial wavelengths of the irregularities. Echoes generated by this process are

expected to contain large wave-normal angles close to the WM resonance cone and hence should exhibit substantial spreading in group delay (≈ 100 ms). We place this echo in the SR category because it is possible that a discrete SR echo that underwent specular reflection at 90 km was “buried” in the diffuse echo.

[70] Figures 12a and 12b show a distinction between signals forward and backscattered by FAIs. In Figure 12a a discrete SR echo appears between 13.5 and 63 kHz with an average time delay of ~ 40 ms and a spread of 3–6 ms at each frequency. This echo is accompanied by diffuse echoes between 25 and 50 kHz with time delays ranging from ~ 40 ms to ~ 80 ms, delays that are greater than those of the discrete elements of the echo. The absence of time delays shorter than those of the discrete elements suggests that the diffuse echoes originated in forward scattering on the return

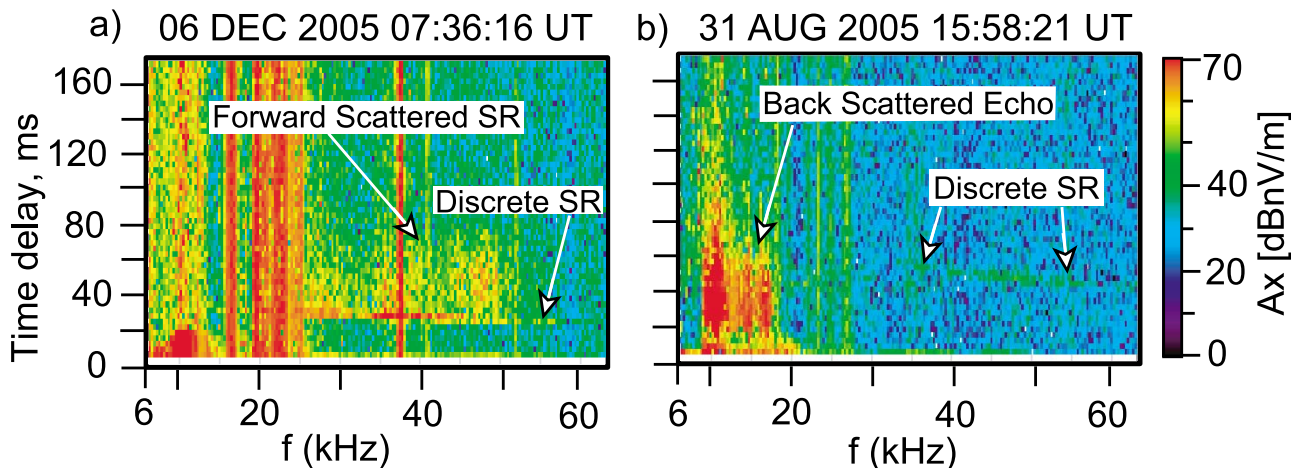


Figure 12. (a) An example of discrete/multipath SR and forward scattered (FS) diffuse SR echoes observed on 6 Dec 2005 (1861 km, $\lambda_m = 56.63^\circ\text{N}$, $L = 4.27$, $\text{MLT} = 9.9$). There is evidence of patchy MR echoes between 10 and 13 kHz. (b) An example of backscattered (BS) diffuse SR echoes and of discrete SR echoes observed on 31 Aug 2005 (1629 km, $\lambda_m = 81.24^\circ\text{N}$, $\text{MLT} = 22.41$).

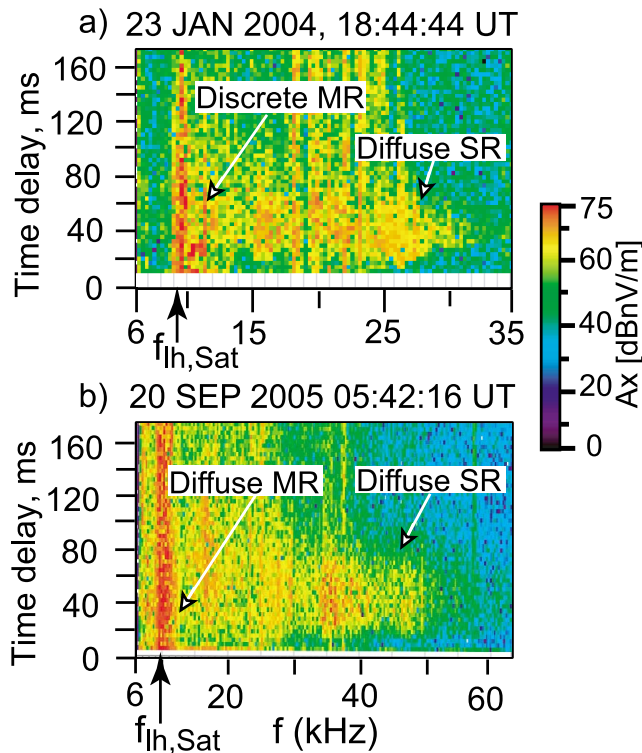


Figure 13. Examples of MR and SR echoes observed at high latitude. (a) Discrete MR echoes accompanied by diffuse SR echoes. (b) Diffuse MR and diffuse SR echoes. There is some evidence of discrete and multipath SR echoes between 30 and 50 kHz.

leg by FAIs close to the satellite. Backscattered waves on the return leg would not be detected. If the downgoing RPI signal also encountered FAIs and was backward and forward scattered as shown in Figure 2d, the backscattered waves did not return to IMAGE, possibly due to Landau damping. Any forward scattered components from the down leg would probably have become weak and indistinguishable parts of the diffuse returning echo.

[71] Figure 12b shows an example of a discrete SR echo between 33 kHz and 63 kHz with time delays ranging from 42 to 57 ms accompanied by a diffuse echo between 9 and 18 kHz with time delays ranging from 15 ms to 67 ms. If the discrete SR echo were observable at lower frequencies, down to 9 kHz, its time delays at lower frequencies would be more than 60 ms, since the travel time of a discrete SR echo typically increases as frequency decreases. This implies that the longest time delay of the diffuse echo at low frequencies was smaller than that of the discrete SR echo, and further implies that the diffuse echoes were produced by backscattering from nearby FAIs. As described by *Sonwalkar et al.* [2004a], the minimum and maximum measured time delays of backscattered echoes provide a basis for estimating the distance of FAIs from the satellite. For example, if we assume typical group velocities of whistler mode waves to be $\sim 30,000$ km/s ($c/10$) for small wave-normal angle waves and ~ 300 km/s ($c/1000$) for waves propagating near the resonance cone (before they undergo Landau damping by ~ 1 eV thermal electrons) the measured minimum and

maximum time delays of 20 ms and 60 ms correspond to FAI distances from IMAGE between 18 and 600 km.

[72] In our observations of diffuse WM echoes we found evidence of forward, backward, and mixed scattering (both types), but forward scattering cases were the most common. We note that similar forward scattering of WM waves near the resonance cone was first observed during intersatellite whistler mode propagation experiments at 0.48 MHz between the two ISIS spacecraft [*James, 1978*].

4.2.3. Diffuse MR and SR Echoes Observed at High Latitude

[73] Both MR and SR echoes observed at high latitude typically exhibited a diffuse signature, indicating the regular presence of small scale FAIs. Figure 13a shows a discrete MR and a diffuse SR echo observed on 23 Jan 2004 (altitude = 2644 km, $\lambda_m = 82^\circ\text{N}$, MLT = 7.6) and Figure 13b diffuse MR and SR echoes observed on 20 Sep 2005 (altitude = 1842 km, $\lambda_m = 84^\circ\text{N}$, MLT = 1.8). The propagation scenarios of these echoes are illustrated in Figures 3a, 2d, 3c, and 2d, respectively. Both MR echoes in Figure 13 had a time delay of ~ 25 ms for the first frequency bin above the bin representing their lower cutoff frequency (note the difference between the two frequency scales). This time delay was a factor of two shorter than the time delays at the corresponding frequencies of the echoes in Figures 5 and 10. In general, the time delay for echoes observed at high latitudes increased more slowly with frequency just above the lower cutoff frequency than did the time delay for echoes observed at lower latitudes. This may have to do with the slope of the f_{lh} curve near the satellite altitude. Even at other frequencies, including the upper cutoff frequency, the time delays were typically shorter than those of the MR echoes shown in Figures 5 and 10. This may be the result of the lower plasma densities frequently found in density cavities at high latitudes. In the case of the MR echo in Figure 13b, another possible reason for lower time delays could be that the IMAGE altitude was 1842 km, quite close to the expected $f_{lh,max1}$ altitudes of 1000–2000 km.

4.2.4. MR- and SR-WM Echoes Seen on Successive Soundings on a Given Orbit

[74] The echoes shown in Figures 10a–10e and 11a–11c were observed on different days. On any given orbit, if IMAGE observed an MR echo on more than one sounding, the trend of the $t_g - f$ trace was generally similar to that shown in Figure 10. Figures 14a–14c show three successive soundings on 22 October 2005. At the higher altitudes a discrete MR echo, with or without a minimum in time delay was observed, followed by multipath and diffuse echoes at lower altitudes. The lower cutoff increased with decreasing altitude. The power of such IMAGE echoes to reveal effects of FAIs is supplemented by the regular presence on the RPI records of signals from ground transmitters exhibiting multipath effects or evidence of spectral broadening in the presence of small scale FAIs.

[75] The echoes from the soundings shown in Figures 14a–14c are separated by $\sim 11^\circ$ in latitude, a result of such soundings being separated in time by 5 min. Had the sounding program been repeated every minute the resolution in latitude would have been 2° . Paper II discusses in detail various experimental and theoretical constraints that determine the spatial resolution achievable for whistler mode sounding.

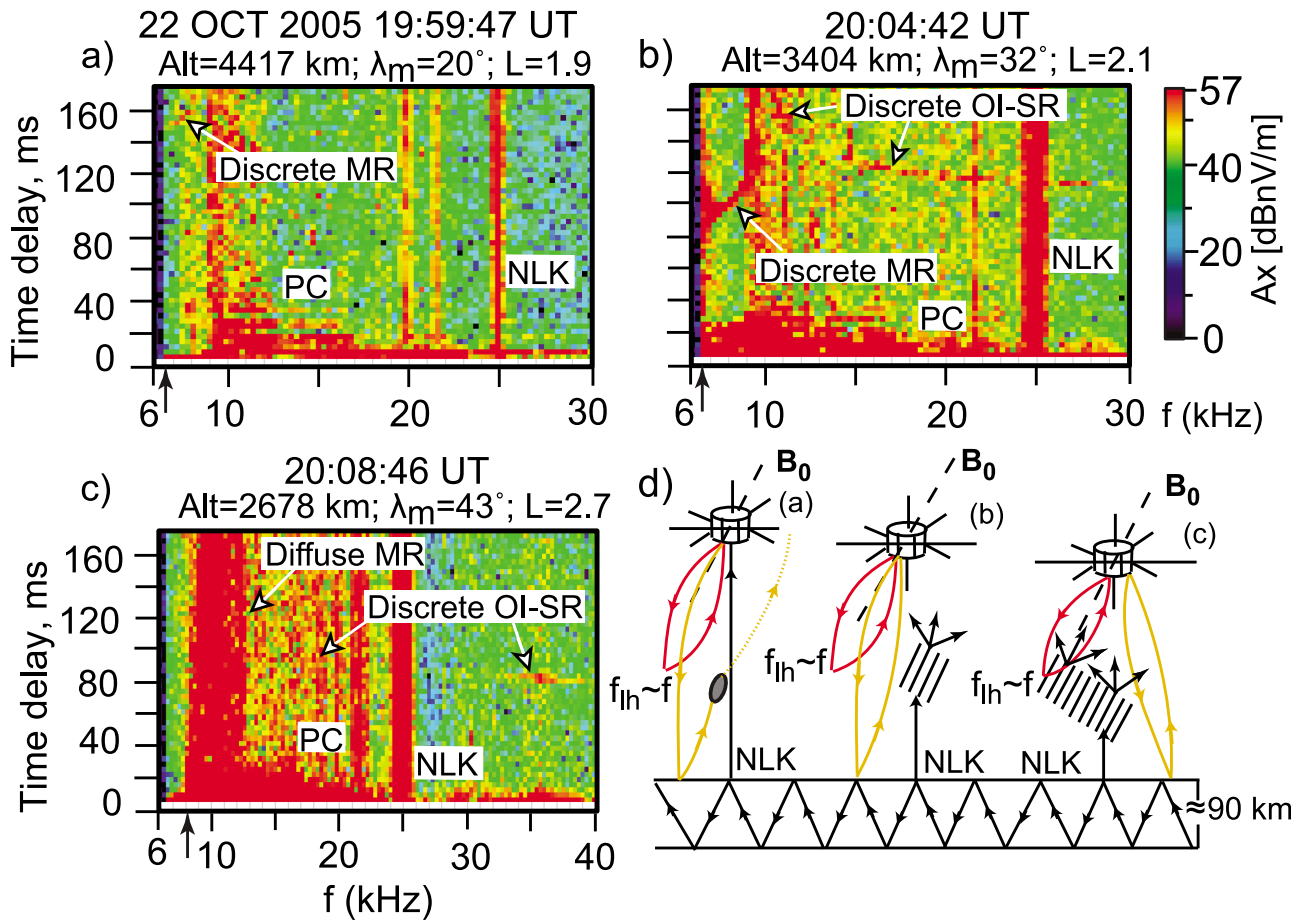


Figure 14. Series of plasmagrams showing MR echoes, SR echoes, and NLK transmitter signals (24.8 kHz, $\Delta f = 0.3$ kHz) on successive RPI soundings extending from $L = 1.9$ to $L = 2.7$ and altitude from 4417 km to 2678 km. (a) At 1959:47 UT, NLK transmitter signals ($\Delta f \sim 300$ Hz) were observed. There is a discrete MR echo between 6.6 and 8.1 kHz. (b) At 2004:42 UT, discrete MR echoes, SR echoes, and NLK transmitter signals appeared. The NLK signals ($\Delta f \sim 1.5$ kHz) showed evidence of spectral broadening. (c) At 2008:46 UT, diffuse MR echoes, discrete SR echoes, and NLK transmitter signals were observed. The NLK signals ($\Delta f \sim 1.5$ kHz) showed evidence of spectral broadening. (d) Schematic showing possible interpretation of the observations in Figures 14a–14c. (See auxiliary material for MR echoes in Figure 14c as seen by Y-antenna.)

[76] Figure 14d shows a possible interpretation of the sequence of echoes shown in Figures 14a–14c. To explain the absence of SR echoes in Figure 14a, we assume that large scale FAIs were present at the L value (1.9) of IMAGE at altitudes lower than where MR echoes reflect. These FAIs deflected the raypaths of those signals that in a smooth magnetosphere would have led to SR echoes but in this case did not return to the satellite. Four minutes later, when the magnetosphere near $L = 2.1$ was smooth, discrete MR and SR echoes were received. A few seconds later RPI received NLK signals that were forward scattered by small scale FAIs and hence were doppler broadened in frequency. Note that in a few seconds, the satellite travels a few tens of kilometers and thus can experience a completely different small scale FAI scenario. Another four minutes later, when IMAGE was at $L = 2.7$, both the MR and NLK signals were affected by small scale FAIs, leading to diffuse MR echoes and spectral broadening of the NLK signal. These FAIs some-

how scattered higher frequency signals so that only a weak SR echo was seen between 30 and 40 kHz.

[77] We believe that such observations can be part of a new diagnostic method. The transmitter signals probe FAIs from below with wave-normals near vertical, while RPI signals can illuminate them from above at all possible radiated wave-normal angles.

4.3. MR and SR Echoes on Three Antennas in 2004 and 2005

[78] After the September 30, 2004 mishap, the echo strengths were about ~ 30 dB stronger on the X- and Z-antennas relative to that on the Y-antenna. This was true of all signals, including PC echoes and ground transmitter signals. Figure 15 shows examples from the three antennas in a pre-mishap case of discrete and diffuse echoes, while Figure 16 shows a post-mishap case of multipath echoes. (The auxiliary material gives three more post-mishap cases of MR echoes from three antennas.)

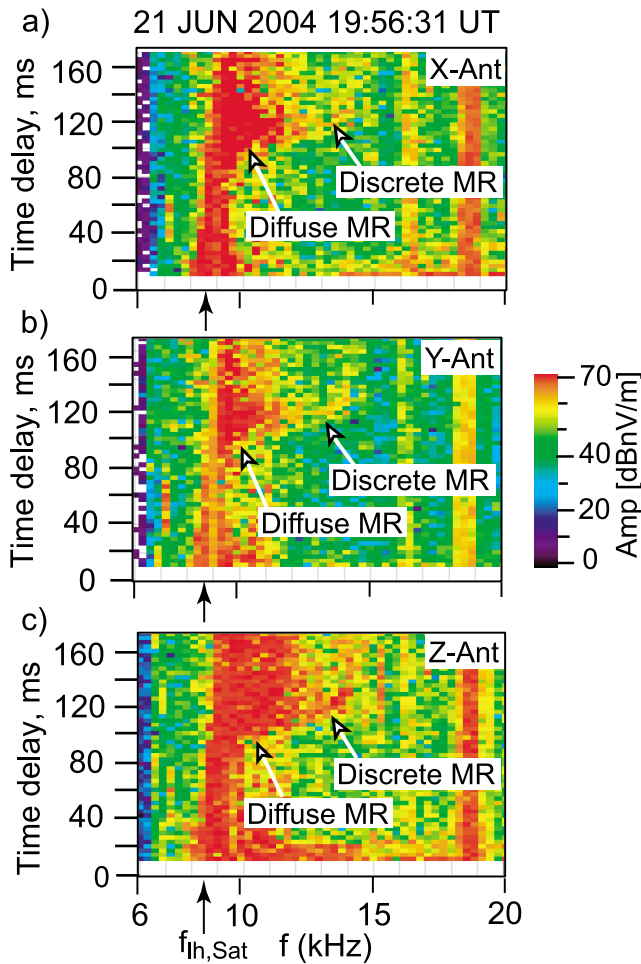


Figure 15. Examples of strong MR echoes observed on the X-, Y-, and Z-antennas on 21 June 2004. Such strong MR echoes were observed on all three antennas before the Y-antenna/receiver mishap on 30 September 2004 (2278.8 km, $\lambda_m = 12.4^\circ\text{N}$, $L = 1.42$, $\text{MLT} = 7.6$). (a) X-antenna (nominal length = 500 m, actual estimated length ~ 340 m), (b) Y-antenna (nominal length = 500 m, actual length unknown), and (c) Z-antenna (nominal length = 20 m).

[79] The failure of the Y-antenna/receiver system provided an unexpected benefit: its reduced sensitivity allowed us to recognize that the vertical diffuse band near 10 kHz on many plasmagrams in fact consisted of MR echoes. In several cases we found that when strong diffuse signals were seen on the X and Z antennas, corresponding signals on the Y antenna were sufficiently weak such that a discrete MR signal could be seen within the band of noise activity. We suggest that this discrete MR echo corresponded to an echo path that the RPI signal would have taken in a hypothetically smooth background magnetosphere, and that the diffuse components resulted from scattering by FAIs.

4.4. Occurrence Pattern of MR and SR Echoes

[80] Probabilities of echo occurrence depend on many factors: radiated power and pattern, antenna orientation, frequency, distance traveled and spreading losses, efficiency of reflection, losses due to absorption (D region), and the

presence of FAIs along the signal raypaths. Figure 17 shows the occurrence patterns along the IMAGE orbit in the geomagnetic meridional plane of various types of WM echoes observed during the transmissions of Program #38 in January-August 2004 and August-December 2005. We saw fewer MR echoes in 2004 because there were fewer transmissions of Program #38. Figure 18 shows the echo activity as a function of maximum K_p ($K_{p,max}$) in the previous 24 hours. The WM echoes described in this paper have been observed at altitudes less than 5,000 km and at all latitudes and during the 3–5 and 8–15 MLT ranges. We believe the altitude limitation was a result of experimental constraints: power transmitted and the maximum time delay limitation of Program #38. The MLT range limitation was the result of IMAGE orbit orientation in space when Program #38 was transmitted. We believe that whistler mode echoes in principle should be observable over a much greater range of altitude and for all MLTs.

[81] The occurrence pattern of SR echoes was in general consistent with the pattern reported earlier [Sonwalkar et al., 2004a]. We observed SR echoes (discrete, multipath, or

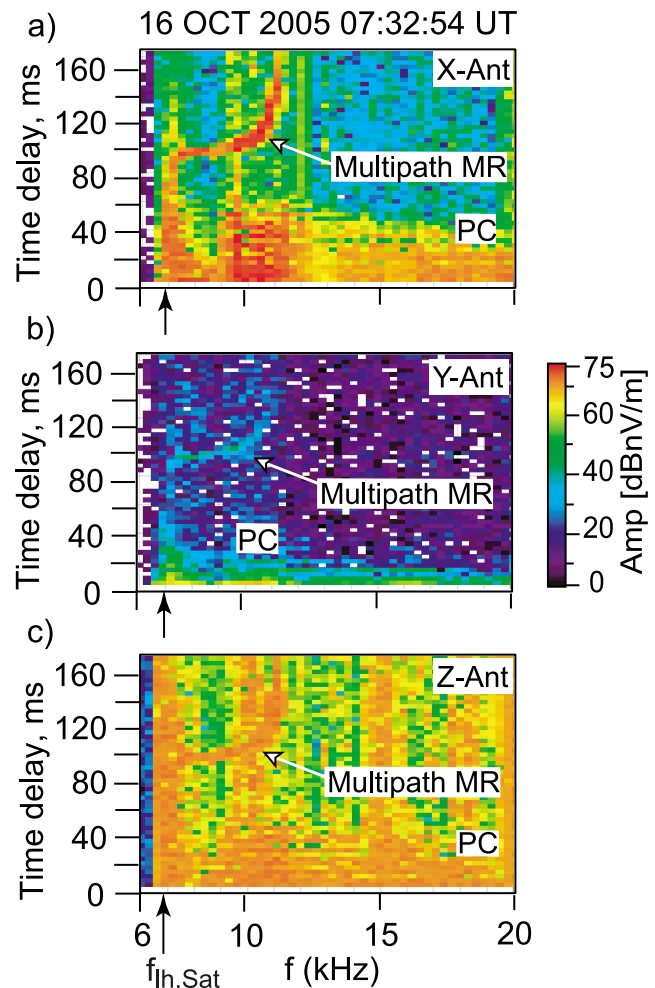


Figure 16. Examples of multipath MR echoes observed on 16 October 2005 (3232 km, $\lambda_m = 22.63^\circ\text{N}$, $L = 1.77$, $\text{MLT} = 12.35$). Strong echoes were observed on the (a) X-antenna and (c) Z-antenna, and weak echoes on the (b) Y-antenna.

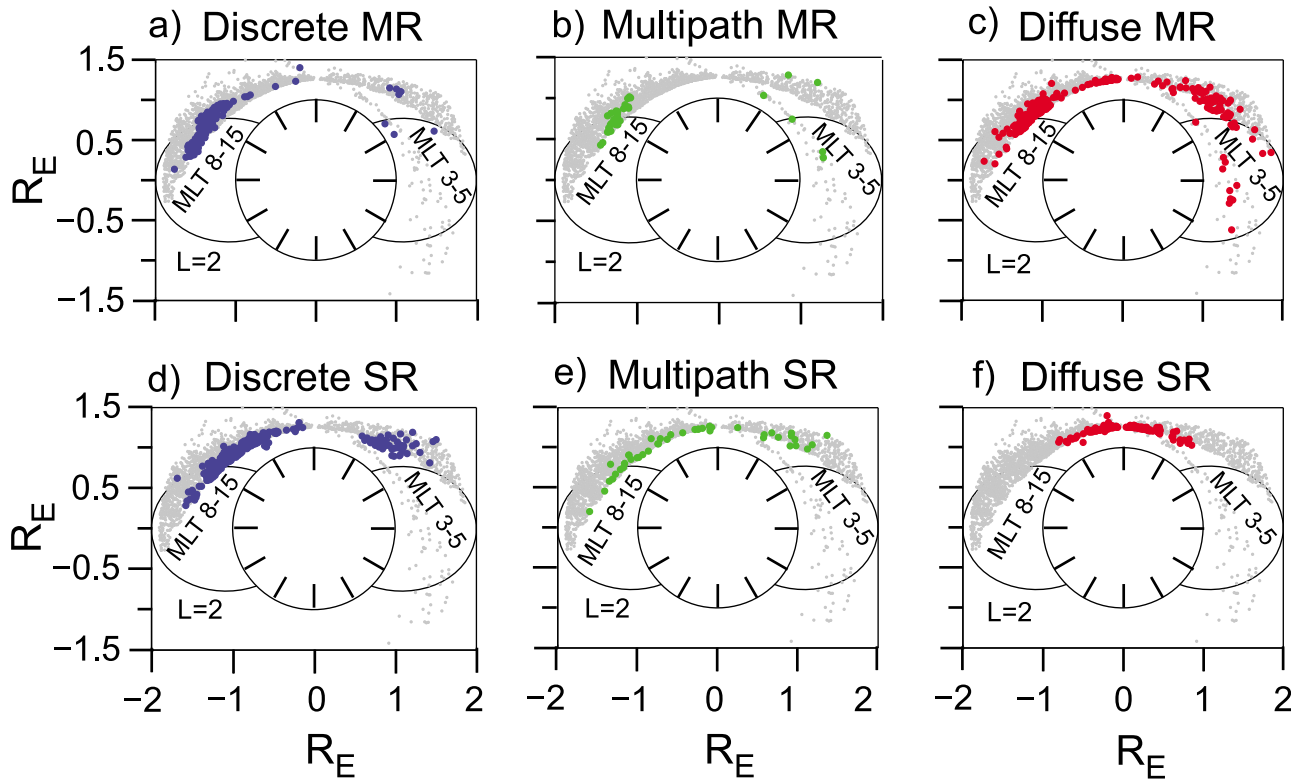


Figure 17. Occurrence pattern of MR echoes and SR echoes in the magnetic meridional plane. Also shown are the satellite orbits and MLT. The gray regions show the locations from which the Program #38 soundings were made. (a) Discrete MR echoes, (b) multipath MR echoes, (c) diffuse MR echoes, (d) discrete SR echoes, (e) multipath SR echoes, and (f) diffuse SR echoes.

diffuse) during ~23% of the transmissions below 5000 km and on at least 50% of the orbits. When observed, such echoes tended to appear on more than one sounding, which were typically spaced by ~2000 km along an orbit (Program #38 was transmitted every ~4 min). We saw discrete SR echoes during 14% of the transmissions, multipath SR echoes during

2%, and diffuse SR echoes during 7% of the transmissions. We observed MR echoes (discrete, multipath, or diffuse) during 20% of the transmissions below 5000 km and on at least 50% of the orbits. We saw discrete MR echoes during 5% of the transmissions, multipath MR echoes during 1%, and diffuse MR echoes during 14%. Though all types of

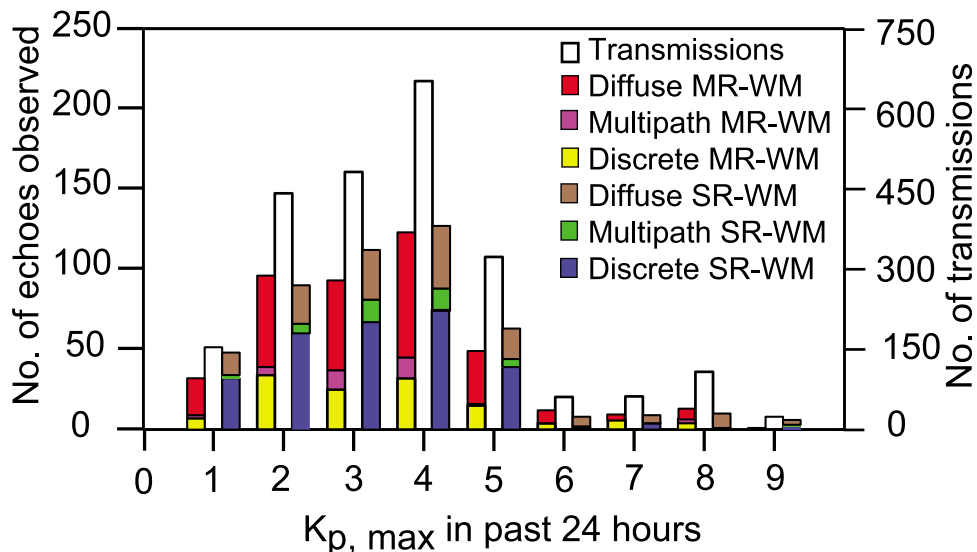


Figure 18. Occurrence pattern of whistler mode echoes as a function of geomagnetic activity.

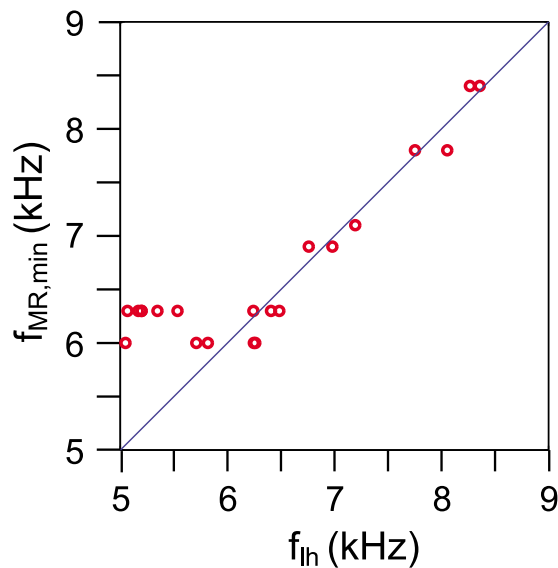


Figure 19. Comparison of f_{lh} , determined from measured f_{uh} and model f_{ce} , with the measured $f_{MR,min}$ of MR echoes. In calculating f_{lh} , it was assumed that $m_{eff} = 1$. Note the minimum value of 6 kHz of $f_{MR,min}$ is set by the lower frequency limit of Program #38.

SR echoes were observed at all latitudes, the largest fraction of discrete echoes was observed at the lower latitudes and the largest fraction of diffuse echoes at higher latitudes. Similarly, all types of MR echoes were observed at all latitudes, but the largest fraction of discrete and multipath MR echoes was observed at the lower latitudes. Diffuse MR echoes were found in large numbers at all latitudes. It is interesting that the most common type of SR echo was the discrete type and the most common type of MR echo the diffuse type.

[82] Over the ~ 5.8 year life of IMAGE mission more than 2500 clearly identifiable whistler mode echoes have been detected. About 450 of these are MR echoes, almost always accompanied by SR echoes, observed mainly during the transmission of Program #38 in 2004 and 2005 as discussed above. The rest are SR echoes. This data set is available for magnetospheric plasma diagnostics discussed in the next section and in Paper II.

5. A New Method to Measure Local f_{lh} , $f_{lh,max1}$, N_e , m_{eff} , and He^+/H^+

[83] If the propagation scenarios outlined in Figures 1–3 are documented by dispersion measurements of observed echoes and supported by propagation theory, including ray tracing, we will have a new method of remotely sensing $f_{lh,max1}$, N_e , m_{eff} , and He^+/H^+ along \mathbf{B}_0 below the satellite while also measuring local f_{lh} . Here we provide a preliminary view of the new method and in Paper II offer propagation-theoretic support of the method as well as two examples of its application.

5.1. Measurement of Local f_{lh} , N_e , m_{eff} , and He^+/H^+

[84] Figure 19 shows a comparison of measured $f_{MR,min}$ with values of f_{lh} calculated from measurements of f_{pe} (interpolated) and model values of f_{ce} . The comparison was based on 13 selected discrete MR cases in the August–

November 2005 period when the RPI dynamic spectra provided unambiguous f_{uh} measurements. Note that the minimum value of $f_{MR,min}$ is set by the minimum transmitted frequency of 6 kHz for Program #38. Given that $f_{MR,min}$ was measured with 300 Hz uncertainty and that f_{pe} was interpolated from values measured a minute before and a minute after Program #38 was transmitted, i.e. interpolated from values of f_{pe} at positions several hundred km from the location where f_{min} was measured, we believe that the match is very good.

[85] Having that $f_{MR,min} = f_{lh}$ from experiment, measurement of $f_{MR,min}$ and equation (1) provide a method to measure m_{eff} , if independent measures of f_{pe} (N_e) and f_{ce} are available. As an example, consider the case of 22 October 2005, when IMAGE was located at 3404 km and $\lambda_m = 31.8^\circ\text{N}$. Using a value of $f_{lh} = 6.3 \pm 0.15$ kHz from the data, $f_{pe} = 584$ kHz obtained from f_{uh} measurements on dynamic spectra, and model value of $f_{ce} = 321$ kHz, we obtain $m_{eff} \approx 1.140$ with $f_{lh} = 6.15$ kHz and obtain $m_{eff} \approx 1.036$ with $f_{lh} = 6.45$ kHz. If we assume that at the satellite the principal contribution to m_{eff} was from H^+ and He^+ , we obtain $He^+/H^+ \sim 0.20$ for $f_{lh} = 6.15$ kHz and $He^+/H^+ \sim 0.05$ for $f_{lh} = 6.45$ kHz. The uncertainty in the m_{eff} and He^+/H^+ measurement is the result of limitations on frequency resolution ($\Delta f = 300$ Hz) for the f_{lh} measurement and uncertainties in f_{pe} and f_{ce} .

[86] On the other hand, measurement of $f_{MR,min} = f_{lh}$ permits measurement of N_e at the satellite location if the satellite is at high enough (>2000 km) altitude such that $m_{eff} \approx 1$. In this case N_e is obtained from equation (1) by using the measured values of $f_{MR,min}$ and f_{ce} either measured or calculated from a model. For example consider the case of 22 Oct 2005, when IMAGE was located at 3404 km and $\lambda_m = 31.8^\circ\text{N}$. Using a value of $f_{lh} = 6.3 \pm 0.15$ kHz from the data, and $f_{ce} = 321$ kHz, we obtain $f_{pe} \approx 462$ kHz with $f_{lh} = 6.15$ kHz and obtain $f_{pe} \approx 543$ kHz with $f_{lh} = 6.45$ kHz.

5.2. Measurements of the Upper and Lower MR Cutoffs: Range of f_{lh} and $f_{lh,max1}$

[87] As mentioned in section 2.1 and demonstrated in Paper II, the upper cutoff, $f_{MR,max}$, of an MR echo is close to but lower than $f_{lh,max1}$ along \mathbf{B}_0 , while the minimum frequency, $f_{OI,min}$, of an OI-SR echo is greater than $f_{MR,max}$ and close to $f_{lh,max1}$ along \mathbf{B}_0 . Depending on the satellite location, $f_{OI,min}$ may be smaller or larger than $f_{lh,max1}$. Figure 20 shows measurements of $f_{MR,min}$ and $f_{MR,max}$, which give the

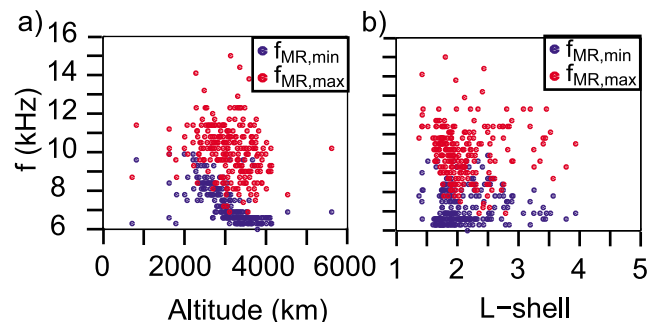


Figure 20. Lower ($f_{MR,min} \approx f_{lh,local}$) and upper cutoff ($f_{MR,max} \approx f_{lh,max1}$) frequencies of MR echoes as a function of (a) altitude and (b) L-shell.

local f_{lh} and the maximum f_{lh} along \mathbf{B}_0 . Typically f_{lh} , as calculated from independently obtained values of f_{pe} and f_{ce} , was within 0.3–0.6 kHz of measured $f_{MR,\min}$ (section 5.1) and, as discussed in Paper II, $f_{lh,\max 1}$ was found to be greater than but within a few hundred Hz of $f_{MR,\max}$ and close to $f_{OL,\min}$. Thus $f_{MR,\max}$ can be used to place a lower bound on $f_{lh,\max 1}$.

[88] Figure 20a shows a plot of $f_{MR,\min} \sim f_{lh,local}$ and $f_{MR,\max} \sim f_{lh,\max 1}$ as a function of satellite altitude and Figure 20b the same as a function of satellite L-shell. Only those cases of MR echoes in which clear lower and upper cutoff measurements could be made were included, thus excluding many diffuse cases observed at high latitude. Relatively few candidate echoes were observed in the auroral region where strong auroral hiss emissions often masked any WM echoes that might have been present. As seen from Figure 20a $f_{lh,local}$ showed a dependence on the satellite altitude, while $f_{lh,\max 1}$ did not. This is expected based on equations (1) and (2) and the dependence of f_{pe} , f_{ce} , and m_{eff} , on altitude (Figure 1). $f_{lh,local}$ varies from 6 to 10 kHz and $f_{lh,\max 1}$ varies from 7 to 15 kHz.

[89] Although measurements of the local lower hybrid frequency have been reported earlier [Barrington *et al.*, 1965; Brice and Smith, 1965], we believe that this is the first remote sensing of $f_{lh,\max 1}$ along geomagnetic field lines. This measurement is significant because it determines the upper frequency cutoff of nonducted WM waves, of man-made or natural origin, that are magnetospherically reflected and can remain trapped in the magnetosphere. It also provides an indirect measure of the $O^+ - H^+$ transition height where O^+ and H^+ ions are in equal numbers. The midlatitude $O^+ - H^+$ transition height is of importance because it corresponds to the transition from the main ionosphere to the plasmasphere [Lemaire and Gringauz, 1998]. As seen from equation (1) and its discussion in section 2.2, $f_{lh,\max 1}$ occurs when m_{eff} starts increasing rapidly. This can also be noticed in Figure 1a. If the $O^+ - H^+$ transition height occurs at higher altitude, m_{eff} would by implication start increasing at higher altitude, and thus give us a lower value of $f_{lh,\max 1}$, since at higher altitude both f_{ce} and f_{pe} are smaller. In Paper II we provide a method to determine m_{eff} along the field line and thus a method to investigate, and with certain assumptions determine, ion composition.

6. Discussion

6.1. WM Sounding at Altitudes Above 4000 km

[90] The diagnostic potential of the LHR in terms of ion composition or effective mass m_{eff} has been demonstrated in passive studies of wave activity observed aboard low altitude polar orbiting satellites [e.g., Barrington *et al.*, 1965; Brice and Smith, 1965] and now once again becomes evident as we investigate active probing at altitudes below ~5000 km with IMAGE. At much higher altitudes, the phenomenon of MR reflection has in the past received considerable attention, but mostly as an aid in modeling the propagation of various VLF waves such as non ducted lightning whistlers [e.g., Edgar, 1976; Walter and Angerami, 1969; Bortnik *et al.*, 2003] and emissions such as chorus [e.g., Bortnik *et al.*, 2008] and hiss [e.g., Sonwalkar and Inan, 1989; Abel and Thorne, 1998]. Now, with the prospect of remotely sensing the distribution of f_{lh} along \mathbf{B}_0 , there is the prospect of using

radio sounding at frequencies lower than the 6 kHz limit of the RPI programs. One could then investigate m_{eff} at altitudes above 4000 km and in particular study the He^+/H^+ ratio near the equator, where contributions of He^+ to the total plasmasphere density of order 10% have made it possible for investigators working with the EUV instrument on IMAGE to use He^+ data as a proxy for the main body of the plasmasphere.

6.2. Need to Include Density Structure in Magnetospheric Wave Propagation Studies

[91] In undertaking studies of wave propagation and wave effects on the radiation belts, such as by use of ray tracing, there is an understandable tendency to assume an initially smooth density distribution, including a relatively smooth plasmopause density profile [e.g., Kimura, 1966; Abel and Thorne, 1998; Starks *et al.*, 2008]. Our studies lend new support to the idea that smooth models should be reconsidered, that for example in plasmaspheric regions at high altitude, cold-plasma-mode waves propagating transverse to \mathbf{B}_0 from the RPI sounder regularly showed evidence of scattering from field aligned density irregularities [e.g., Carpenter *et al.*, 2002]. In this work we found evidence that plasmaspheric and ionospheric regions below ~5000 km were regularly populated by density structure that perturbed VLF propagation paths from the RPI sounder. These structures, varying in terms of their specific effects, must be considered in modeling the propagation and reflection of waves such as ducted and nonducted whistlers and natural waves and emissions that approach low altitude regions from above. It is difficult to imagine achieving satisfactory models of WM wave levels in the magnetosphere without such considerations.

[92] A probable consequence of FAIs is the development at low altitudes of a trapped randomized population of VLF waves which may (through chance coherence) give rise to new emissions and may in turn set a noise threshold for wave particle interactions between electrons and coherent waves (transmitter signals) or quasi-coherent waves (lightning whistlers).

6.3. Augmentation of Wave Injection Experiments in Space by Transmissions From Ground-Based Transmitters

[93] Our work suggests that ground based transmitter signals can substantially augment WM injection experiments in space by providing reference information on waves injected at specific locations and at roughly vertical wave-normal angles.

[94] The effective length of antennas in space plasmas is an important but poorly known quantity [Sonwalkar and Inan, 1986; James, 2006]. This problem has acquired a special importance because a recent study [Starks *et al.*, 2008] shows that there may be a 10–20 dB discrepancy between the electric fields of ground transmitter signals as measured on satellites and as determined by propagation theories. Observations of ground transmitter signals by the three antennas on IMAGE provide ample opportunity to determine the antenna effective lengths of the broken X and Y antennas relative to that of the Z-antenna as a function of frequency, plasma parameters, orientation and direction of propagation of the incident wave

[95] *Sonwalkar et al.*, 2004b]. The knowledge of the relative values of the effective lengths of the three antennas is required to determine the wave polarization, which then can be used to determine the wave-normal directions of echoes arriving at the satellite [*Sonwalkar et al.*, 2001].

6.4. Notes on the Effects of FAIs

[95] Having identified the principal echo forms likely to occur within the context of field line distributions such as depicted in Figure 1, it became possible to see the types of complexity that FAIs can impose on the propagation scenarios. For example, on looping paths, a returning signal may be deflected or scattered in such a way as to miss the spacecraft altogether, as suggested by the dotted curves in Figures 2b, 2d, 3b, 3c, 3e, and 3f. Such effects could cause patchiness in the continuity of multipath echoes. The NI echo, following a raypath that is not aligned with \mathbf{B}_0 , may encounter, and be scattered or deflected by, small or large scale irregularities on field lines not encountered by the OI echo. This may help account for the comparative rarity of NI traces. In the case of backscattered echoes by FAIs close to the satellite; these echoes do not involve reflections. Their observed dispersion is generally different from that of any of the standard WM echo types to the extent that they cannot be regarded as mere modifications of the standard MR or SR echoes. Such BS echoes often start with minimum time delays, or in the MR case do not show a sharp cutoff and can be best interpreted as scattering of RPI signals by FAI close to the satellite.

6.5. Reassurance About Basic Propagation Concepts and a Surprise

[96] There have been elements of reassurance as well as of surprise in our study. In terms of predicting the zeroth order effects, we were pleased to find that, on average, in a system as complex as the magnetosphere, the observed WM echoes display properties (e.g. cutoffs, dispersion t_g vs f) consistent with those predicted by plane wave propagation in a smooth model magnetoplasma in diffusive equilibrium (along \mathbf{B}_0). The expected maximum in f_{lh} in the 1000–2000 km range associated with the rapid increase in m_{eff} led to an understandable variety of MR echoes. Unexpected, however, was the OI-SR echo that is obliquely (as opposed to normally) incident during reflection at the ionospheric lower boundary and which then follows a looping path back to the sounder (the NI echoes were to be expected, based on a rather flat and abrupt earth-ionosphere boundary [*Sonwalkar et al.*, 2001]). This behavior, detailed in Paper II, was found to be attributable to the “right” type of ray bending of certain large-wave-normal waves propagating through the density gradients of the F layer.

7. Summary and Conclusions

[97] A survey of echoes detected in 2004–2005 during pulse transmissions from the RPI instrument on the IMAGE satellite has revealed several new features of sounder generated whistler mode (WM) echoes and demonstrated ways in which the echoes may be used for remote sensing of the Earth’s plasma structure at altitudes below ~5000 km. Based on their reflection mechanisms, the echoes can be classified as: magnetospherically reflected (MR), specularly reflected (SR), or backscattered (BS).

[98] The MR echoes are reflected at altitudes where the local lower hybrid frequency (f_{lh}) is equal to the transmitted pulse frequency f , a phenomenon familiar from both theory and passive recordings of WM wave activity. The raypath forms a loop because of the transverse (to \mathbf{B}_0) orientation of the wave vector at the altitude of reflection. The $f - t_g$ profile of an MR echo provides information on how f_{lh} , and hence the plasma composition (ion effective mass m_{eff}) is distributed between the satellite and a (usually) lower altitude in the 1000–2000 km range where f_{lh} reaches a peak value along \mathbf{B}_0 .

[99] The SR echoes (previously reported in a higher frequency range) are reflected at the Earth-ionosphere boundary at 90 km, either with wave vector at normal incidence (the NI echo) or, more commonly (due to ray bending in the layered ionosphere), at oblique incidence (the OI echo). The OI echo path forms a loop that remains close to the field line of the satellite, while the NI reflection point is displaced from that field line. The $f - t_g$ profiles of OI and NI echoes are sensitive to the distribution of electron density between the satellite and the bottom of the ionosphere.

[100] The BS echoes are the result of diffuse reflections from small scale plasma density irregularities close to IMAGE.

[101] The various echo $f - t_g$ forms are described as discrete, multipath, and diffuse, according to the amount of travel-time spreading that they exhibit on plasmagrams. The discrete WM echoes with relatively small spreading in time delays (<5–10 ms) at each frequency are believed to occur when the plasma density distribution along the geomagnetic field \mathbf{B}_0 passing through IMAGE is relatively smooth. The multipath echoes with medium spreading in time delays (~10–30 ms) at each frequency occur when large scale (~1–10 km) field aligned irregularities (FAIs) are present near \mathbf{B}_0 . The diffuse echoes with large spreading in time delays (>30–40 ms) occur when small scale (~10 m–100 m) field aligned irregularities (FAIs) are present near \mathbf{B}_0 . We distinguish diffuse SR or MR echoes from BS echoes; the first two have undergone reflections at the Earth-ionosphere boundary and magnetospheric reflection, respectively, whereas the third has not.

[102] The diagnostic potential of these phenomena for remotely studying the distribution of plasma density and composition along \mathbf{B}_0 , as well as the presence of FAIs of varying scale sizes, is enhanced by the tendency for SR and MR echoes to be observed simultaneously and in company with upward propagating signals from a spatial distribution of communication VLF transmitters. Overall, we believe that our findings about WM propagation and echoing in an irregular medium have important implications for the connection between WM waves and the Earth’s radiation belts.

[103] **Acknowledgments.** The work at University of Alaska Fairbanks was supported by NASA under contracts NNG04GI67G and NNX08AN51A. Authors thank Robert Benson for many useful discussions.

[104] Robert Lysak thanks Csaba Ferencz and another reviewer for their assistance in evaluating this paper.

References

Abel, B., and R. M. Thorne (1998), Electron scattering loss in Earth’s inner magnetosphere: 2. Sensitivity to model parameters, *J. Geophys. Res.*, *103*, 2397–2407.

- Barrington, R. E., J. S. Belrose, and G. L. Nelms (1965), Ion composition and temperature at 1000 km as deduced from simultaneous observations of a VLF plasma resonance and topside sounding data from the Alouette I satellite, *J. Geophys. Res.*, *70*, 1647–1664.
- Bell, T., and H. Ngo (1988), Electrostatic waves stimulated by coherent VLF signals propagating in and near the inner radiation belt, *J. Geophys. Res.*, *93*, 2599–2618.
- Bell, T. F., and H. D. Ngo (1990), Electrostatic lower hybrid waves excited by electromagnetic whistler mode waves scattering from planar magnetic field-aligned irregularities, *J. Geophys. Res.*, *95*, 149–172.
- Bell, T. F., H. G. James, U. S. Inan, and J. P. Katsufakis (1983), The apparent spectral broadening of VLF transmitter signals during transionospheric propagation, *J. Geophys. Res.*, *88*, 4813–4840.
- Benson, R. F., P. A. Webb, J. L. Green, L. Garcia, and B. W. Reinisch (2004), Magnetospheric electron densities inferred from upper-hybrid band emissions, *Geophys. Res. Lett.*, *31*, L20803, doi:10.1029/2004GL020847.
- Bortnik, J., U. S. Inan, and T. F. Bell (2003), Frequency time spectra of magnetospherically reflected whistlers in the plasmasphere, *J. Geophys. Res.*, *108*(A1), 1030, doi:10.1029/2002JA009387.
- Bortnik, J., R. M. Thorne, and N. P. Meredith (2008), The unexpected origin of plasmaspheric hiss from discrete chorus emissions, *Nature*, *452*, 62–66.
- Brice, N. M., and R. L. Smith (1965), Lower hybrid resonance emissions, *J. Geophys. Res.*, *70*, 71–80.
- Brittain, R., P. M. Kintner, M. C. Kelley, J. C. Siren, and D. L. Carpenter (1983), Standing wave patterns in VLF hiss, *J. Geophys. Res.*, *88*, 7059–7064.
- Burch, J. L. (2000), IMAGE mission overview, *Space Sci. Rev.*, *91*, 1–14.
- Carpenter, D., N. Dunckel, and J. Walkup (1964), A new very low frequency phenomenon: Whistlers trapped below the protonosphere, *J. Geophys. Res.*, *69*, 5009–5017.
- Carpenter, D. L., M. A. Spasojevic, T. F. Bell, U. S. Inan, B. W. Reinisch, I. A. Galkin, R. F. Benson, J. L. Green, S. F. Fung, and S. A. Boardsen (2002), Small-scale field-aligned plasmaspheric density structures inferred from the Radio Plasma Imager on IMAGE, *J. Geophys. Res.*, *107*(A9), 1258, doi:10.1029/2001JA009199.
- Carpenter, D. L., T. F. Bell, D. Chen, D. Ng, C. Baran, B. W. Reinisch, and I. Galkin (2007), Proton cyclotron echoes and a new resonance observed by the Radio Plasma Imager instrument on the IMAGE satellite, *J. Geophys. Res.*, *112*, A08208, doi:10.1029/2006JA012139.
- Cerisier, J. C. (1973), A theoretical and experimental study of non-ducted VLF waves after propagation through the magnetosphere, *J. Atmos. Terr. Phys.*, *35*, 77–94.
- Edgar, B. C. (1976), The lower and upper-frequency cutoffs of magnetospherically reflected whistlers, *J. Geophys. Res.*, *81*, 205–211.
- Fejer, B. G., and M. C. Kelley (1980), Ionospheric irregularities, *Rev. Geophys.*, *18*(2), 401–454.
- Groves, K., M. Lee, and S. Kuo (1988), Spectral broadening of VLF radio signals traversing the ionosphere, *J. Geophys. Res.*, *93*, 14,683–14,687.
- Helliwell, R. A. (1965), *Whistlers and Related Ionospheric Phenomena*, Stanford Univ. Press, Stanford, Calif.
- James, H. G. (1972), Refraction of whistler-mode waves by large-scale gradients in the middle latitude ionosphere, *Ann. Geophys.*, *28*(2), 301–309.
- James, H. (1978), Wave propagation experiments at medium frequencies between two ionospheric satellites: 2. Whistler-mode pulses, *Radio Sci.*, *13*, 543–558.
- James, H. G. (2006), Dipole measurements of waves in the ionosphere, *Lect. Notes Phys.*, *687*, 191–210.
- Kimura, I. (1966), Effects of ions on whistler-mode ray tracing, *Radio Sci.*, *1*, 269–283.
- Lemaire, J. F., and K. I. Gringauz (1998), *The Earth's Plasmasphere*, Cambridge Univ. Press, Cambridge, U. K.
- Muldrew, D. G. (1969), Nonvertical propagation and delayed-echo generation observed by the topside sounders, *Proc. IEEE*, *57*, 1097–1107.
- Persoon, A. M., D. A. Gurnett, and S. D. Shawhan (1983), Polar cap electron densities from DE 1 plasma wave observations, *J. Geophys. Res.*, *88*, 10,123–10,136.
- Persoon, A. M., D. A. Gurnett, W. K. Peterson, J. H. Waite Jr., J. L. Burch, and J. L. Green (1988), Electron density depletions in the nightside auroral zone, *J. Geophys. Res.*, *93*, 1871–1895.
- Rastani, K., U. Inan, and R. Helliwell (1985), DE 1 observations of Siple transmitter signals and associated sidebands, *J. Geophys. Res.*, *90*, 4128–4140.
- Reinisch, B. W., et al. (2000), The Radio Plasma Imager investigation on the IMAGE spacecraft, *Space Sci. Rev.*, *91*, 319–359.
- Shklyar, D. R., M. Parrot, J. Chum, O. Santolik, and E. E. Titova (2010), On the origin of lower- and upper-frequency cutoffs on wedge-like spectrograms observed by DEMETER in the midlatitude ionosphere, *J. Geophys. Res.*, *115*, A05203, doi:10.1029/2009JA014672.
- Siren, J. (1975), Fast hissers in substorms, *J. Geophys. Res.*, *80*, 93–97.
- Smith, R. (1964), An explanation of subprotonospheric whistlers, *J. Geophys. Res.*, *69*, 5019–5021.
- Smith, R., and J. Angerami (1968), Magnetospheric properties deduced fromOGO 1 observations of ducted and nonducted whistlers, *J. Geophys. Res.*, *73*, 1–20.
- Sonwalkar, V. S. (2006), The influence of plasma density irregularities on whistler-mode wave propagation, *Lect. Notes Phys.*, *687*, 141–191.
- Sonwalkar, V., and J. Harikumar (2000), An explanation of ground observations of auroral hiss: Role of density depletions and meter-scale irregularities, *J. Geophys. Res.*, *105*, 18,867–18,883.
- Sonwalkar, V., and U. Inan (1986), Measurements of Siple transmitter signals on the DE 1 satellite: Wave-normal direction and antenna effective length, *J. Geophys. Res.*, *91*, 154–164.
- Sonwalkar, V. S., and U. S. Inan (1989), Lightning as an embryonic source of VLF hiss, *J. Geophys. Res.*, *94*, 6986–6994.
- Sonwalkar, V. S., T. F. Bell, R. A. Helliwell, and U. S. Inan (1984), Direct multiple path propagation: A fundamental property of nonducted VLF waves in the magnetosphere, *J. Geophys. Res.*, *89*, 2823–2830.
- Sonwalkar, V. S., X. Chen, J. Harikumar, D. L. Carpenter, and T. F. Bell (2001), Whistler-mode wave injection experiments in the plasmasphere with a radio sounder, *J. Atmos. Sol. Terr. Phys.*, *63*, 1199–1216.
- Sonwalkar, V. S., et al. (2004a), Diagnostics of magnetospheric electron density and irregularities at altitude <5000 km using whistler and Z mode echoes from radio sounding on the IMAGE satellite, *J. Geophys. Res.*, *109*, A11212, doi:10.1029/2004JA010471.
- Sonwalkar, V., J. Li, R. Proddaturi, A. Venkatasubramanian, D. Carpenter, R. Benson, and B. Reinisch (2004b), Interpretation of vector electric field measurements by RPI using three dipole antennas on IMAGE, *Eos Trans. AGU*, *85*(47), Fall Meet. Suppl., Abstract SM23A-0465. [Available at <http://adsabs.harvard.edu/abs/2004AGUFMSM23A0465S>.]
- Sonwalkar, V. S., D. L. Carpenter, R. Proddaturi, A. Reddy, and B. Reinisch (2006), Observations of magnetospherically reflected (MR) whistler mode (WM) echoes observed by Radio Plasma Imager (RPI) on the IMAGE satellite: Diagnostics of electron density and ion composition, *Eos Trans. AGU*, *87*(52), Fall Meet. Suppl., Abstract SM11B-0323. [Available at <http://adsabs.harvard.edu/abs/2006AGUFMSM11B0323S>.]
- Sonwalkar, V. S., A. Reddy, D. L. Carpenter, and B. Reinisch (2007), Observations of magnetospherically reflected (MR), specularly reflected (SR), and back scattered (BS) whistler mode (WM) echoes observed by Radio Plasma Imager (RPI) on IMAGE: Diagnostics of electron density, density structure, and ion composition, *Eos Trans. AGU*, *88*(52), Fall Meet. Suppl., Abstract SM32A-04. [Available at <http://adsabs.harvard.edu/abs/2007AGUFMSM32A..04S>.]
- Sonwalkar, V. S., A. Reddy, D. L. Carpenter, and B. W. Reinisch (2008a), Whistler mode sounding of the magnetosphere: Measurement of electron density, ion composition (H^+ , He^+ , O^+), and density irregularities along the geomagnetic field, paper presented at 2008 Commission G XXIXth General Assembly, Int. Union of Radio Sci., Chicago, Ill., 7–16 August.
- Sonwalkar, V. S., A. Reddy, D. L. Carpenter, and B. W. Reinisch (2008b), The physical principles of the generation of whistler mode echoes by a radio sounder (RPI) on a spacecraft (IMAGE), *Eos Trans. AGU*, Fall Meet. Suppl., *89*(53), Abstract SM33A-1765. [Available at <http://adsabs.harvard.edu/abs/2008AGUFMSM33A1765S>.]
- Sonwalkar, V. S., S. Hazra, K. Mayank, A. Reddy, D. L. Carpenter, and B. W. Reinisch (2009), Whistler mode echoes observed below 2,000 km altitude by Radio Plasma Imager (RPI) on IMAGE: Radio sounding of electron density and ion composition (H^+ , He^+ , O^+), *Eos Trans. AGU*, Fall Meet. Suppl., *90*(52), Abstract SM44A-05. [Available at <http://adsabs.harvard.edu/abs/2009AGUFMSM44A..05S>.]
- Sonwalkar, V. S., A. Reddy, and D. L. Carpenter (2011), Magnetospherically reflected, specularly reflected, and backscattered whistler mode radio-sounder echoes observed on the IMAGE satellite: 2. Sounding of electron density, ion effective mass (m_{eff}), ion composition (H^+ , He^+ , O^+), and density irregularities along the geomagnetic field line, *J. Geophys. Res.*, *116*, A11211, doi:10.1029/2011JA016760.
- Starks, M. J., R. A. Quinn, G. P. Ginet, J. M. Albert, G. S. Sales, B. W. Reinisch, and P. Song (2008), Illumination of the plasmasphere by terrestrial very low frequency transmitters: Model validation, *J. Geophys. Res.*, *113*, A09320, doi:10.1029/2008JA013112.
- Titova, E. E., V. I. Di, V. E. Yurov, O. M. Raspopov, V. Y. Trakhtengertz, F. Jiricek, and P. Triska (1984), Interaction between VLF waves and the turbulent ionosphere, *Geophys. Res. Lett.*, *11*(4), 323–326.
- Walter, F., and J. Angerami (1969), Nonducted mode of VLF propagation between conjugate hemispheres: Observations onOGO's 2 and 4 of the

“walking-trace” whistler and of Doppler shifts in fixed frequency transmissions, *J. Geophys. Res.*, 74, 6352–6370.

D. L. Carpenter, Space, Telecommunications and Radioscience Laboratory, Stanford University, Stanford, CA 94305, USA. (dlc@nova.stanford.edu)

S. Hazra, K. Mayank, R. Proddaturi, A. Reddy, and V. S. Sonwalkar, Electrical and Computer Engineering Department, University of Alaska Fairbanks, PO Box 755915, Fairbanks, AK 99775, USA. (shazra@alaska.edu; kmayank@alaska.edu; venkat-radha-krish.proddaturi@keane.com; areddy1@alaska.edu; vssonwalkar@alaska.edu)

B. W. Reinisch, Center for Atmospheric Research, University of Massachusetts Lowell, Lowell, MA 01845, USA. (bodo_reinisch@uml.edu)